



HAL
open science

Numerical workflow for scale-resolving computations of space launcher afterbody flows with and without jets

Jolan Reynaud, Pierre-Elie Weiss, Sebastien Deck

► **To cite this version:**

Jolan Reynaud, Pierre-Elie Weiss, Sebastien Deck. Numerical workflow for scale-resolving computations of space launcher afterbody flows with and without jets. *Computers and Fluids*, 2021, 226, pp.104994. 10.1016/j.compfluid.2021.104994 . hal-03321498

HAL Id: hal-03321498

<https://hal.science/hal-03321498>

Submitted on 17 Aug 2021

HAL is a multi-disciplinary open access archive for the deposit and dissemination of scientific research documents, whether they are published or not. The documents may come from teaching and research institutions in France or abroad, or from public or private research centers.

L'archive ouverte pluridisciplinaire **HAL**, est destinée au dépôt et à la diffusion de documents scientifiques de niveau recherche, publiés ou non, émanant des établissements d'enseignement et de recherche français ou étrangers, des laboratoires publics ou privés.

Numerical workflow for scale-resolving computations of space launcher afterbody flows with and without jets

J. Reynaud^{1a}, P-E. Weiss^{2a}, S. Deck^{3a}

^aONERA-The French Aerospace Lab, 8 rue des Vertugadins 92190 Meudon (France)

Abstract

Scale resolving numerical methods are necessary to accurately predict the afterbody flows of space launchers. Numerical workflows built for such computations have to be designed in order to obtain a minimal numerical dissipation to resolve fine turbulent structures, a sufficient robustness to capture eventual shock waves and both a reasonable computational cost and an acceptable user workload enabling comparative design studies. This article presents the development of a hybrid numerical framework based on Ducros’s sensor and designed to switch from a low-dissipation formulation in presence of vortical structures to a robust formulation around high gradients. This hybrid workflow is used with ZDES, including its latest automatic mode (ZDES mode 2 (2020)), to simulate a transonic space launcher afterbody experiment with and without a cold air propulsive jet [1] [2]. The salient physical properties of the base flow are investigated and the evaluation of computed results follows the extended nomenclature for validation of simulation techniques [3] from level 0 to 5. The framework is thus validated for instantaneous and mean flow visualizations, base and extension mean pressure coefficient distribution, pressure fluctuation levels, one-point and two-point spectral analyses. Such an efficient automatic RANS/LES strategy could be well suited to study realistic launcher afterbody geometries with propulsive jet(s).

Keywords: ZDES, Hybrid scheme, base flow, jet interactions, compressible flows, AUSM, turbulent flows, space launcher

1. Introduction

1.1. Space launcher base flow phenomenology

The prediction of the afterbody flow of a space launcher during its flight is of primary importance for the correct assessment of the aerodynamic performance and the stability of the vehicle, especially in order to establish new designs such as reusable launchers. In flight, the massively separated turbulent flow behind the base and around the nozzle(s) induces two major phenomena: base drag and side-loads. First, base drag, mainly due to the low pressure recirculation zone forming behind the base constitutes a significant contribution to the overall drag. Then, side-loads (related to the buffeting phenomena), caused by pressure fluctuations linked to the large-scale unsteady motion of the recirculation bubble, influence the flight stability and may cause vibrations of the mechanical structures. These adverse effects, especially strong in the high subsonic regime ($M_\infty=0.5-0.9$), may furthermore be enhanced by the

¹jolan.reynaud@onera.fr

²Corresponding author : pierre-elie.weiss@onera.fr

³sebastien.deck@onera.fr

interaction between the propulsive jet(s) and the base flow. This interaction is composed of a blocking effect (non-viscous) and of an entrainment effect (viscous and turbulent). The blocking effect is related to the shape of the jet which acts as a solid wall deflecting the external flow. The entrainment effect tends to empty the base region and thus to decrease base pressure as the jet entrains the external flow through a mixing layer. The main features of the flow are shown on Fig.1 for a subsonic case of a cylindrical extension behind an axisymmetric forebody.

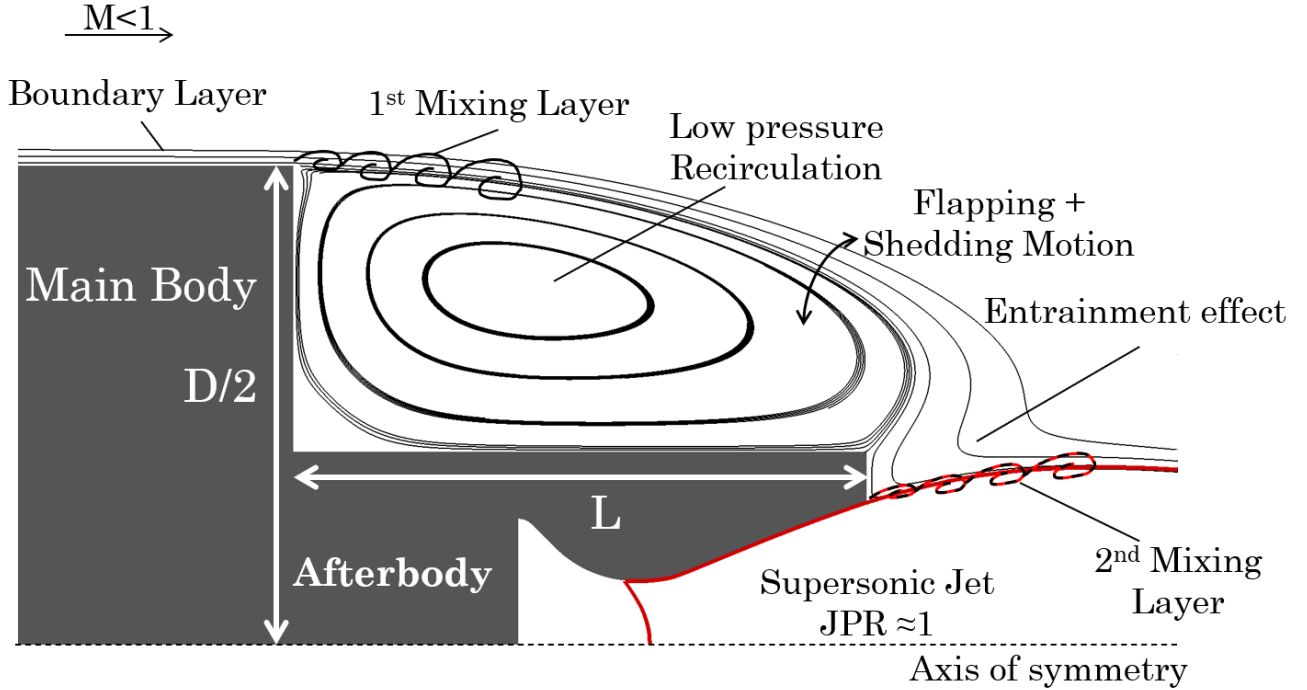


Figure 1: Topology of the interactions between a propulsive jet and a subsonic base flow

1.2. Review of quantitative studies

The phenomenology qualitatively described in sub-section 1.1 has been studied for decades [4] and gives a practical framework to study base flows. However it has to be noticed that a thorough quantitative characterization of a space launcher afterbody aerodynamics, for instance according to the extended nomenclature for validation of simulation techniques [3] shown in Tab 1, demands high fidelity spatio-temporal methods which are complex and costly to use for both experimental and numerical studies. Hence, the literature showing qualitative results for unsteady quantities of the high subsonic flow around an axisymmetric backward facing step is quite recent as shown in Tab.2 which is not exhaustive but provides an overview of the state of the art. Examining this review, one can see that most efforts have been focused on long extension ratio $\frac{L}{D} \geq 1.2$ (D : base diameter, L : extension length) representative of Ariane 5 whereas designs presented for the Ariane 6 and Ariane Next [5] rockets indicate choices in favour of much shorter extensions $\frac{L}{D} \leq 0.6$. These studies also tend to focus on side loads and the base drag issue was given less attention. Furthermore, numerical studies including a propulsive jet are still rare [6] [7]. We propose here a numerical study on a relatively short extension geometry ($L/D=0.6$) with and without a propulsive jet and with interest on both static and dynamic base pressure properties.

| Grade | Levels of validation |
|-------|--|
| 0 | Instantaneous flowfield visualization (coherent structure criteria, numerical schlieren) |
| 1 | Integral forces (lift, drag and pitch) |
| 2 | Mean aerodynamic field (velocity or pressure profiles) |
| 3 | Second-order statistics (r.m.s. quantities) |
| 4 | One-point spectral analysis (power spectral densities) |
| 5 | Two-point spectral analysis (correlation, coherence and phase spectra) |
| 6 | High-order and time-frequency analysis (time-frequency, bicoherence spectra) |

Table 1: Extended nomenclature for levels of validation of simulation techniques [3] adapted from [8].

| Study | Afterbody (L/D) | Mach Number | Method | Jet |
|---------------------------------|-------------------------|--------------|-------------------|-----|
| Depres (2003) [2] [1] | 0.6/1.2 | 0.6/0.7/0.85 | Exp | Yes |
| Le (2005) [9] | 0.15/0.28/.../1.08/1.22 | 0.7/0.8 | Exp | Yes |
| Deck and Garnier (2005) [10] | 0.6 | 0.7 | ZDES and LES | Yes |
| Deck and Thorigny (2007) [6] | 1.2 | 0.7 | ZDES | Yes |
| Meliga and Reijasse (2007) [11] | 1.2 | 0.7/0.9 | Exp | - |
| Weiss et al. (2009) [12] | 1.2 | 0.7 | ZDES | - |
| Weiss and Deck (2011) [13] | 1.2 | 0.7 | ZDES | - |
| Bitter et al. (2011) [14] | ∞ | 0.7 | Exp | - |
| Bitter et al. (2012) [15] | ∞ | 0.7 | Exp | - |
| Statnikov et al. (2013) [16] | ∞ | 0.7 | RANS/LES | - |
| Pain et al. (2014) [17] | 1.2/boosters | 0.7 | ZDES | - |
| Pont et al. (2014) [18] | 1.2 | 0.7 | RANS/LES and ZDES | - |
| Schrijer et al. (2014) [19] | 2.54 | 0.7 | Exp | - |
| Scharnowski et al. (2015) [20] | ∞ | 0.7 | Exp and RANS/LES | - |
| Statnikov et al. (2017) [7] | 1.2 | 0.8 | RANS/LES | Yes |
| Horchler et al. (2018) [21] | 1.2 | 0.7 | IDDES and ZDES | - |
| Van Gent (2018) [22] | 0.6/0.9/1.2/1.8 | 0.76 | Exp | Yes |
| Scharnowski et al. (2019) [23] | ∞ | 0.76 | Exp | - |
| Saile (2019) [24] | 0.45/0.6/0.9/1.05/1.2 | 0.8 | Exp | Yes |

Table 2: Overview of studies on high subsonic base flows over axisymmetric generic geometries. Exp : Wind-tunnel experiments. Adapted from [22]

30 1.2.1. Physical characterization of high-subsonic base flow

Several physical observations characterizing high-subsonic base flows based on the aforementioned literature have been gathered in this section.

Beginning with static observations, the mean base pressure coefficient (C_{p_b}) was shown to be mostly radially

invariant and does not depend on M_∞ for axisymmetric cases without jet. Values of Cp_b are usually measured around -0.15 for case with $L/D=1.2$ [1] [24] and -0.12 for a canonic axisymmetric base flow ($L=0$) [4]. Such values testify of an important base drag. In the presence of a propulsive jet, Cp_b is lowered [1] [10], this decrease is less important when the extension is longer [9]. Regarding the reattachment length of the recirculation bubble, a growth is observed together with M_∞ for cases without jet [22] [24]. For $M_\infty=0.8$, the reattachment of the recirculation bubble is solid (i.e. occurs on the extension) for $L/D \geq 0.9$ and is hybrid or fluid (i.e. occurs downstream of the extension) for shorter extensions [9] [24]. Furthermore, the reattachment length is shortened in the presence of a propulsive jet [22] [24].

Based on spectral analysis and modal decomposition applied on wall pressure signals or numerical data, the dynamic behaviour of an axisymmetric base flow can be decomposed into different main motions. The Strouhal number based on the base diameter $St_D = \frac{fD}{U_\infty}$ is used to characterize fluctuations occurring at frequency f . Authors have observed a low characteristic frequency ($St_D \leq 0.1$) corresponding to a lateral pumping motion and linked to the growth and decay of the whole recirculation bubble. This frequency is dominant for pressure fluctuations near the base [12][7]. An antisymmetric vertical motion due to a vortex shedding phenomena at a reduced frequency $St_D \approx 0.2$ has also been found [1][6][12][7][22]. The vortex shedding frequency is dominant along the extension and the energy of global effort fluctuations is concentrated near it [12] [25]. The harmonics of these two low frequency peaks can also be observed on pressure signals. The recirculation region is also moved by fluctuations with a broadband spectrum centered in $St_D \approx 0.5-0.6$. These fluctuations are attributed to vortical structures formed by Kelvin-Helmoltz instabilities in the shear layer of the recirculation zone [6] [12]. To complete this description, authors showed that, in the presence of a long extension or a jet, the base flow tends to be stabilized and the amplitude of the antisymmetric oscillations at the vortex shedding frequency is reduced [1] [6] [24]. Moreover, it has been observed that, even though the jet modifies significantly the turbulent kinetic energy distribution of the base flow only for short extensions [22], pressure fluctuations (estimated with Cp_{rms}) on the base and on the extension are usually higher in the presence of a jet due to its aeroacoustic noise [24] for all extension lengths.

1.2.2. Turbulence modelling strategies

Thanks to the numerical studies presented in Tab.2 and others on blunt base flows [26][27], several results regarding the choice of turbulence modelling strategies for base flow computations can be summarized here. First, most RANS turbulence models are not well suited for base flow computations. They usually produce an acceptable qualitative flow topology but fail to provide correct mean wall pressure values, recirculation lengths and velocity distribution in the recirculation zone [26][10][28]. The resolution of large eddies driving the dynamics of separated flows is required to increase the representativeness of unsteady base flow simulations [10]. Nevertheless, full Large Eddy Simulations (LES) have almost not been used on such geometries because of the computational cost linked to very fine mesh requirements for attached boundary layers and the long-time sampling needed to capture low frequency dynamics [10]. Strategies enabling to treat attached boundary layer in RANS mode and the separated flow in LES-like mode have then been favoured in the literature [6][21][18] [23][20]. Two main approaches are available for this purpose, providing a good compromise between accuracy and computational cost. A first category encompasses hybrid methods in which the framework ensure a continuous transition from RANS to LES

equations. Good results on canonical and realistic geometries have been obtained with the ZDES (Zonal Detached Eddy Simulation) approach [29] which is based on the Spalart-Allmaras (SA) model [30] and has been used for space launcher aerodynamics in [6][12][17][3][31], with the IDDES (Improved Delayed Detached Eddy Simulation) and the SAS (Scale Adaptive Simulation) approach which are based on Menter’s $k - \omega$ model [32] and have been
75 respectively used in [21] and [18] and with the PG (Perot and Gadebusch [33]) turbulence model which is based on the standard $k - \epsilon$ and has been used in [18]. Then, a second family of approaches gathers coupling methods where information taken from a RANS zone is used as inlet conditions for a LES zone, often through an overlapping zone. Such approaches have been successfully used on semi-complex geometries [16][20][7] with a MILES [34] formulation .

80 The present study will use the ZDES approach for turbulence modelling, including its latest automatic mode (ZDES mode 2 (2020) [35]) in order to promote a low user workload numerical framework.

1.3. Numerical strategies

For the RANS/LES formulations previously described, the accuracy of the numerical scheme has been shown to be of primary importance. Indeed, reducing the numerical dissipation enables to resolve smaller turbulent
85 scales, to limit the influence of the modelled turbulence diffusion on the computed flow and to avoid the damping of instabilities thus improving the transition from RANS to fully developed LES zones. However, lowering the numerical dissipation tends to decrease the robustness of a method and increases the risk of numerical divergence, especially when strong shocks are present. For this reason, computations including a propulsive jet (containing shock cells) have often used a robust scheme, degrading the resolution of turbulent structures compared to plume-
90 off cases. Among the numerical studies of Tab.2, for cases without propulsive jet, modified versions of the AUSM+ scheme [36] including a centered contribution have been used on structured grids with second-order [16] and third-order (MUSCL reconstruction) accuracies [12] [17]. For cases with jet, for which shock cells have to be resolved, authors have either kept this type of scheme and used very fine grids [7](500M points) or switched to more robust schemes like Roe’s scheme [10][6] for coarser grids (≈ 10 M points) with a noticeable loss in scale resolution in
95 comparison with jet-off cases. On unstructured grids, Godunov-type methods, even enhanced with high order k-exact reconstruction, appeared too dissipative and required very fine grids to solve turbulent structures accurately. That is why an hybrid centered/upwind version of these methods is proposed in [18]. This scheme uses Ducros’s sensor [37] to detect vortical regions to apply the centered version of the scheme. A sensor is thus used here to locally reduce numerical dissipation.

100 As described in [38], this idea of optimizing dynamically the numerical resolution of the flow based on local properties, especially for turbulent flows containing shocks, is still an open subject of the literature. To develop such a framework, adapted to complex flows on curvilinear geometries, one can study fundamental works on academic shock/turbulence configurations dedicated to the development and the evaluation of high-order shock-capturing formulations [37][39][40][41][42][38]. The proposed methods are mainly suited for uniform cartesian grids but they
105 provide a thorough analysis of numerical challenges to overcome and promote inspiring sensor formulations that can be customized for specific configurations.

In this study, we propose a hybrid numerical formulation for curvilinear grids based on Ducros’s sensor [37] that

is able to switch from a low-dissipation formulation in presence of vortical structures to a robust formulation in presence of high gradients.

110 1.4. Organization of the paper

The paper is organized as follows: in Section 2 we describe the physical models chosen to conduct the study, their numerical implementation is then detailed in Section 3. The test case and the meshing strategy are presented in Section 4 and the computational results are finally analyzed in Section 5.

2. Physical modelling

115 2.1. Governing equations

To describe the compressible gas flows of interest in this study, one can use the general conservative form of the averaged/filtered Navier Stokes equations:

$$\frac{\partial \mathbf{w}_c}{\partial t} + \text{div}(\mathcal{F}) = \text{div}(\mathcal{G}) \quad (1)$$

$\mathbf{w}_c = {}^t(\rho, \rho \mathbf{V}, \rho E)$ denotes the vector of conservative quantities. ρ is the gas density, $\mathbf{V} = {}^t(u, v, w)$ is the velocity vector of the flow and E represents the total energy of the gas. \mathcal{F} and \mathcal{G} denote respectively the convection and diffusion terms:

$$\mathcal{F} = {}^t(\rho \mathbf{V}, \rho \mathbf{V} \otimes \mathbf{V} + P \bar{\mathbf{I}}, (\rho E + P) \mathbf{V}) \quad (2)$$

$$\mathcal{G} = {}^t(0, \bar{\bar{\tau}}^*, \bar{\bar{\tau}}^* \cdot \mathbf{V} - \mathbf{q}^*) \quad (3)$$

with P the thermodynamic pressure, $\bar{\bar{\tau}}^*$ the combination of the viscous stress and the modelled turbulent stress (Reynolds or subgrid) tensors:

$$\tau_{ij}^* = 2(\mu + \mu_t)(S_{ij} - \frac{1}{3}\delta_{ij}S_{ii}) \quad i, j = 1..3 \quad (4)$$

$$S_{ij} = \frac{1}{2}\left(\frac{\partial u_i}{\partial x_j} + \frac{\partial u_j}{\partial x_i}\right) \quad i, j = 1..3 \quad (5)$$

120 with μ and μ_t being the dynamic viscosity and the modelled turbulent viscosity which is provided by a turbulence model. $\mathbf{q}^* = \mathbf{q} + \mathbf{q}_t$ is the total heat flux with \mathbf{q} the laminar heat flux computed with Fourier's law and \mathbf{q}_t the modelled turbulent heat flux linked to μ_t by a turbulent Prandtl number.

2.2. Turbulence modelling with Zonal Detached Eddy Simulation (ZDES)

ZDES is a multiresolution approach developed by ONERA [29][43] which aims at treating in a simple model all classes of flow problems indicated in Fig 2. In this formulation, three specific hybrid length scale formulations (see Eq. (6)) also called modes are optimized to be employed on three typical flowfield topologies as illustrated in Fig 2 . In the frame of the SA model, \tilde{d}_{ZDES} replaces the distance to the wall d_w according to:

$$\tilde{d}_{ZDES} = \tilde{d}_{mode} \left(\tilde{\Delta}, d_w, U_{i,j}, \nu, \tilde{\nu}, \frac{\partial \tilde{\nu}}{\partial n}, \frac{\partial ||\omega||}{\partial n} \right) \quad (6)$$

$$mode = 1, 2, 3 \quad (7)$$

with $\tilde{\Delta}$ denoting the subgrid length scale entering \tilde{d}_{ZDES} that depends on the grid cell size, $U_{i,j}$ the velocity gradients, d_w the distance to the wall, $||\omega||$ the magnitude of vorticity, ν and $\tilde{\nu}$ the kinematic and pseudo eddy viscosity as well as $\frac{\partial \tilde{\nu}}{\partial n}$ the derivative in the wall-normal direction. The definition of \tilde{d}_{ZDES} is not a minor adjustment
 130 in the DES framework since the modified lengthscales depend not only on the grid but also on the velocity and eddy viscosity fields and their wall-normal derivatives. ZDES takes full advantage of its zonal nature since complex configurations can be accurately treated by the use of various formulations within the same calculation (an example is provided in [44]).

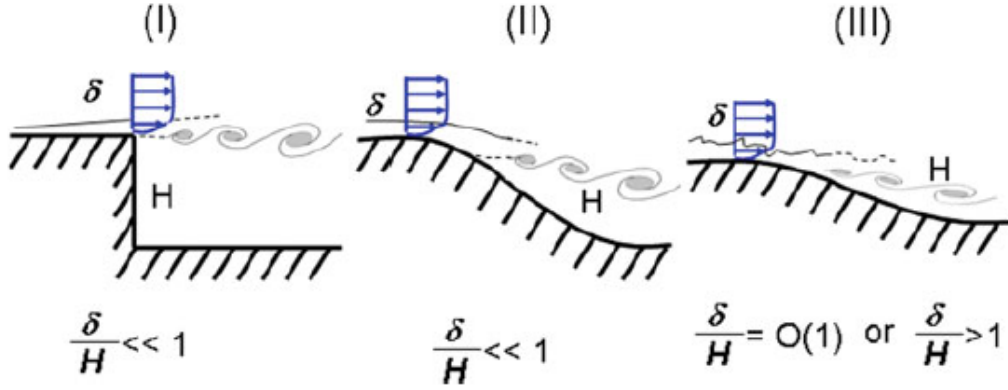


Figure 2: Classification of typical flow problems. I: separation fixed by the geometry, II: separation induced by a pressure gradient on a curved surface, III: separation strongly influenced by the dynamics of the incoming boundary layer

To study generic axisymmetric base flows for which the separation is clearly fixed by the geometry, the mode
 135 1 of the ZDES is an appropriate choice, it will be used in this study. However, when studying more realistic space launcher geometries as in [3][45], determining the separation point *a priori* can be difficult and the use of a completely automatic RANS/LES formulation such as the mode 2 of the ZDES is needed. To this end, the latest development of the automatic mode of ZDES, referred to as ZDES mode 2 (2020) [35] will be assessed in this study as well.

140 3. Numerical Methods

3.1. Discrete formulation

We used the FLU3M solver [46] developed by ONERA to solve the compressible Navier-Stokes equations on multiblock structured grids. An implicit finite volume form of the governing equations (Eq.(1)), based on Gear's second-order accurate time discretization, yields for a hexahedral cell centered in (i,j,k) with a volume Ω_{ijk} :

$$\begin{aligned} \frac{3}{2}\Delta(\mathbf{w}_c)_{ijk}^{n+1} - \frac{1}{2}\Delta(\mathbf{w}_c)_{ijk}^n + \frac{\Delta t}{\Omega_{ijk}} \sum_{l=1}^6 (\mathbf{F}(\mathbf{w}_c) - \mathbf{G}(\mathbf{w}_c))_{ijk,l}^n = \\ - \frac{\Delta t}{\Omega_{ijk}} \sum_{l=1}^6 \left[\left(\frac{\partial \mathbf{F}(\mathbf{w}_c)}{\partial \mathbf{w}_c} - \frac{\partial \mathbf{G}(\mathbf{w}_c)}{\partial \mathbf{w}_c} \right)_{ijk,l}^n \Delta(\mathbf{w}_c)_{ijk}^{n+1} \right] \end{aligned} \quad (8)$$

Where n and $n+1$ represent consecutive time steps and $\Delta(\mathbf{w}_c)_{ijk}^{n+1} = (\mathbf{w}_c)_{ijk}^{n+1} - (\mathbf{w}_c)_{ijk}^n$. For each interface l associated to a normal vector $\mathbf{n}=\hat{t}$ (n_x, n_y, n_z) and a surface $\Delta S_{ijk,l}$, the discrete convective and diffusive fluxes \mathbf{F} and \mathbf{G} are defined as:

$$\mathbf{F}(\mathbf{w}_c)_{ijk,l} = \begin{pmatrix} \rho(\mathbf{V} \cdot \mathbf{n}) \\ \rho u(\mathbf{V} \cdot \mathbf{n}) + P n_x \\ \rho v(\mathbf{V} \cdot \mathbf{n}) + P n_y \\ \rho w(\mathbf{V} \cdot \mathbf{n}) + P n_z \\ (\rho E + P)(\mathbf{V} \cdot \mathbf{n}) \end{pmatrix}_{ijk,l} \cdot \Delta S_{ijk,l} \quad (9)$$

$$\mathbf{G}(\mathbf{w}_c)_{ijk,l} = \begin{pmatrix} 0 \\ \tau_{xx}^* n_x + \tau_{xy}^* n_y + \tau_{xz}^* n_z \\ \tau_{xy}^* n_x + \tau_{yy}^* n_y + \tau_{yz}^* n_z \\ \tau_{xz}^* n_x + \tau_{yz}^* n_y + \tau_{zz}^* n_z \\ \bar{\tau}^* \cdot \mathbf{V} - \mathbf{q}^* \cdot \mathbf{n} \end{pmatrix}_{ijk,l} \cdot \Delta S_{ijk,l} \quad (10)$$

In order to use Eq.(8) to compute $(\mathbf{w}_c)_{ijk}^{n+1}$ at the center of cells grid knowing $(\mathbf{w}_c)_{ijk}^n$, we thus have to choose numerical procedures to evaluate $\mathbf{F}(\mathbf{w}_c)_{ijk,l}$, $\mathbf{G}(\mathbf{w}_c)_{ijk,l}$ and there Jacobian matrices $\left(\frac{\partial \mathbf{F}(\mathbf{w}_c)}{\partial \mathbf{w}_c}\right)_{ijk,l}^n, \left(\frac{\partial \mathbf{G}(\mathbf{w}_c)}{\partial \mathbf{w}_c}\right)_{ijk,l}^n$ at the interface between cells.

150 To assess the Jacobian matrices we use the procedure detailed by Pechier in [47] [48]. Furthermore, to evaluate the diffusion flux vector \mathbf{G} , values of $\rho, D^*, \mu^*, \lambda^*, \mathbf{V}, h_i$ at the cell interface are needed, the average of the right and left center values are used to estimate them. Estimations of velocity and temperature gradients are needed as well. To this end, a corrected Green-Gauss approach described in [49] is used. It is designed to prevent numerical instabilities that can arise due to odd-even decoupling oscillations allowed by the original Green-Gauss approach.

155 Finally, two numerical features will be used to evaluate convective fluxes, namely a numerical scheme and a numerical procedure designed to increase the scheme accuracy: the MUSCL reconstruction method. On the basis of the literature review displayed in Sec.1.3, we propose here a hybrid numerical scheme formulation blending the low-dissipation AUSM+(P)[50] and the original AUSM+ [36] combined with different MUSCL reconstruction strategies. The hybridisation is based on the use of Ducros's sensor [37] to detect zones featuring shock waves in order to add numerical dissipation locally. The idea here is to preserve the good scale resolution properties of the low-dissipation AUSM+(P) scheme in vortical regions and to enhance its robustness near shocks. The different aspects of this framework are detailed below.

3.2. Numerical scheme

3.2.1. Low-dissipation AUSM+(P)

Mary and Sagaut [50] proposed a simplified formulation of the AUSM+(P) designed to ensure a low numerical dissipation. We recall here the main features of this scheme. For the sake of explanation, we suppose that we are willing to compute this low dissipation (LD) flux $\mathbf{F}_{j+\frac{1}{2}}^{LD}$ through the interface between the cell (i,j,k) and the cell $(i,j+1,k)$. The Euler fluxes are approximated by :

$$\mathbf{F}_{j+\frac{1}{2}}^{LD} = V_1 \frac{\Psi_L + \Psi_R}{2} - |U_{dis}| \frac{\Psi_R - \Psi_L}{2} + P_1 \quad (11)$$

With $\Psi_{L,R}$ being the left and right states obtained at the interface with the chosen MUSCL reconstruction (described in Sec.3.3). V_1 corresponds to the interface fluid velocity and $P_1 = [0, \frac{P_L+P_R}{2}n_x, \frac{P_L+P_R}{2}n_y, \frac{P_L+P_R}{2}n_z, 0]$. U_{dis} is a parameter based on the local fluid velocity to control the numerical dissipation. More precisely, V_1 is computed with a pressure stabilization term:

$$V_1 = \frac{(\mathbf{V}_L + \mathbf{V}_R) \cdot \mathbf{n}}{2} - c_2(P_R - P_L), \quad (12)$$

and U_{dis} is defined as:

$$U_{dis} = \zeta * \max\left(\left|\frac{(\mathbf{V}_L + \mathbf{V}_R) \cdot \mathbf{n}}{2}\right|, c_1\right) \quad (13)$$

165 c_1 and c_2 are constant parameters based on the flow reference values ($c_1 = 0.04 * U_\infty$ and $c_2 = 0.04 * \frac{1}{U_\infty \rho_\infty}$) and $\zeta \in \{0; 1\}$ is a sensor used to minimize dissipation by enabling a fully centered scheme in monovariant zones [50].

As explained earlier, this scheme has been used with success on various cases but is not adapted for flow configurations leading to strong shocks. For the case with propulsive jet studied here, this scheme, used with a 3rd-order MUSCL reconstruction, leads to a rapid numerical divergence. This is also the case when:

- 170 • The scheme is used with a 2nd-order MUSCL reconstruction.
- The scheme is used with ζ forced to 1 and with a 2nd-order MUSCL reconstruction.

As explained in Sec1.3, we want to enhance locally the dissipation of this scheme. One idea is to blend this formulation with another numerical scheme providing good shock capturing properties. To this end we chose the AUSM+ formulation described here after.

175 3.2.2. AUSM+

The AUSM+ scheme has been proposed by Liou [36]. The main idea here is to decompose the non-viscous fluxes $\mathbf{F}(\mathbf{w}_c)$ between convective fluxes $\mathbf{F}^{(c)}$ and acoustic fluxes \mathbf{P} .

$$\mathbf{F}(\mathbf{w}_c) = \mathbf{F}^{(c)} + \mathbf{P} \quad (14)$$

$$\mathbf{F}^{(c)} = Ma^t(\rho, \rho\mathbf{V}, \rho H), \quad \mathbf{P} = {}^t(0, P_x, P_y, P_z, 0) \quad (15)$$

$M = \frac{\mathbf{V} \cdot \mathbf{n}}{a}$, a the speed of sound and H the total enthalpy ($H = E + \frac{P}{\rho}$).

We need to express a convective flux $\mathbf{f}_{j+1/2}^{(c)}$ and a pressure flux $\mathbf{p}_{j+1/2}$. Defining $a_{j+1/2}$ as the speed of sound at the cell interface, one can express:

$$\mathbf{f}_{j+1/2}^{(c)} = m_{j+1/2} a_{j+1/2} \Psi_{j+1/2}, \quad \Psi = {}^t(\rho, \rho\mathbf{V}, \rho H) \quad (16)$$

and

$$\mathbf{p}_{j+1/2} = {}^t(0, P_x, P_y, P_z, 0)_{j+1/2} \quad (17)$$

$\Psi_{j+1/2}$ is given by a basic upwinding procedure:

$$\Psi_{j+1/2} = \begin{cases} \Psi_L & \text{if } m_{j+1/2} \geq 0 \\ \Psi_R & \text{otherwise} \end{cases} \quad (18)$$

The terms $m_{j+1/2}$, $\mathbf{p}_{j+1/2}$ and $a_{j+1/2}$ have yet to be defined. Liou [36] introduces a decomposition of these terms as the sum of two contributions:

$$m_{j+1/2} = \mathcal{M}^+(M_j) + \mathcal{M}^-(M_{j+1}) \quad (19)$$

$$\mathbf{p}_{j+1/2} = \mathcal{P}^+(M_j)\mathbf{p}_j + \mathcal{P}^-(M_{j+1})\mathbf{p}_{j+1} \quad (20)$$

Liou [36] proposes the forms:

$$\mathcal{M}^\pm(M) = \begin{cases} \frac{1}{2}(M \pm |M|), & \text{if } |M| \geq 1 \\ \pm \frac{1}{2}(M \pm 1)^2 \pm \frac{1}{8}(M^2 - 1)^2 & \text{otherwise} \end{cases} \quad (21)$$

$$\mathcal{P}^\pm(M) = \begin{cases} \frac{1}{2}(1 \pm \text{sign}(M)), & \text{if } |M| \geq 1 \\ \pm \frac{1}{4}(M \pm 1)^2(2 \pm M)^2 \pm \frac{3}{16}M(M^2 - 1)^2 & \text{otherwise} \end{cases} \quad (22)$$

with $\text{sign}(M) = \frac{M}{|M|}$. For the speed of sound at the interface, a simple average yields satisfying results:

$$a_{j+1/2} = \frac{1}{2}(a_j + a_{j+1}) \quad (23)$$

180 The AUSM+ numerical flux $\mathbf{F}_{j+\frac{1}{2}}^{AU}$ is finally computed as:

$$\mathbf{F}_{j+\frac{1}{2}}^{AU} = m_{j+1/2}a_{j+1/2}\Psi_{j+1/2} + \mathbf{p}_{j+1/2} \quad (24)$$

3.2.3. Hybrid shock capturing scheme

To ensure both a low numerical dissipation and good local shock capturing properties, we propose the following hybrid formulation:

$$\mathbf{F}_{j+\frac{1}{2}} = (1 - \beta)\mathbf{F}_{j+\frac{1}{2}}^{LD} + \beta\mathbf{F}_{j+\frac{1}{2}}^{AU} \quad (25)$$

With β a sensor designed to detect shocks, based on Ducros's [37] sensor Φ :

$$\Phi = \frac{(\nabla \cdot \mathbf{u})^2}{(\nabla \cdot \mathbf{u})^2 + (\nabla \wedge \mathbf{u})^2 + \epsilon} \quad \epsilon = 1.10^{-32}s^{-2} \quad (26)$$

$\nabla \cdot \mathbf{u}$ is the divergence of the velocity vector, it takes high values near shocks and $\nabla \wedge \mathbf{u}$ evaluates the vorticity of the flow, it takes high values in vortical regions. Thus, $\Phi \in [0; 1]$ and it takes values close to one near a shock wave and close to zero in vortical regions. A more complete formulation has been derived to enhance dissipation near shocks, to maintain β between 0 and 1 and to ensure a smooth variation of β limiting sensitivity to numerical instabilities:

$$\beta(\Phi) = \tanh(c * \Phi) \quad (27)$$

As shown in Fig.3, the choice of $c=3$ for the constant value provides a good compromise. Indeed, this value ensures a high β value plateau near shock waves (Φ close to 1) while maintaining low values of $\beta(\Phi)$ in vortical region where usually $\Phi \leq 0.01$, for instance $\beta(0.01) \approx 0.03$.

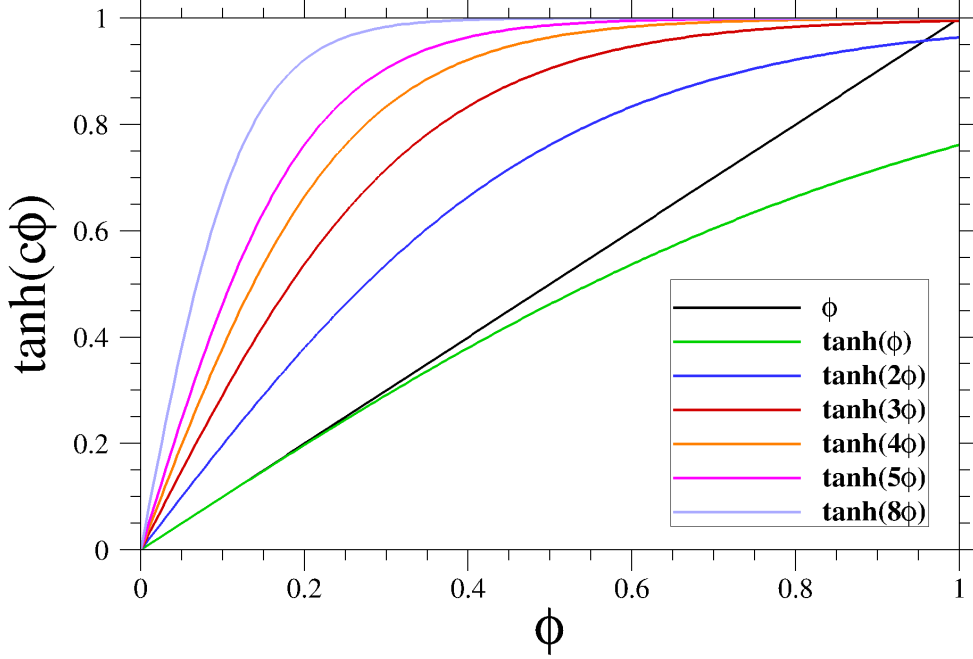


Figure 3: Evolution of function $\tanh(c * \Phi)$ for different values of c .

185 3.3. MUSCL reconstruction strategy

To complete the description of the numerical scheme presented above, the procedure providing the left and right states $\Psi_{L,R}$ at the interface has to be clarified.

3.3.1. Slope computation

As explained in [51][52][53], if one simply uses the center values $\Psi_L = (\mathbf{w}_c)_{i,j,k}^n$ and $\Psi_R = (\mathbf{w}_c)_{i,j+1,k}^n$ to compute $\mathbf{F}_{j+\frac{1}{2}}$, the presented numerical scheme would only be first order accurate in space. In order to enhance the scheme accuracy, Van Leer [54] has proposed the MUSCL strategy (Monotonic Upstream-centered Scheme for Conservation Law) which consists in considering a linear variation of state variables inside cells instead of using constant values as shown in Fig.4. For a variable w of the vector (\mathbf{w}_c) , two types of evaluations can be used to compute the slope of variations inside the cells:

$$\text{Upwind} : \begin{cases} w_{j+\frac{1}{2}}^L = w_j + \frac{w_j - w_{j-1}}{2} \\ w_{j+\frac{1}{2}}^R = w_{j+1} - \frac{w_{j+2} - w_{j+1}}{2} \end{cases} \quad (28)$$

$$\text{Centered} : \begin{cases} w_{j+\frac{1}{2}}^L = w_j + \frac{w_{j+1} - w_j}{2} \\ w_{j+\frac{1}{2}}^R = w_{j+1} - \frac{w_{j+1} - w_j}{2} \end{cases} \quad (29)$$

The general framework of the MUSCL reconstruction method consists in a combination of the two mentioned methods thanks to a parameter κ :

$$\begin{cases} w_{j+\frac{1}{2}}^L = w_j + \frac{1-\kappa}{4}\Delta_{j-\frac{1}{2}} + \frac{1+\kappa}{4}\Delta_{j+\frac{1}{2}} \\ w_{j+\frac{1}{2}}^R = w_{j+1} - \frac{1+\kappa}{4}\Delta_{j+\frac{1}{2}} - \frac{1-\kappa}{4}\Delta_{j+\frac{3}{2}} \end{cases} \quad (30)$$

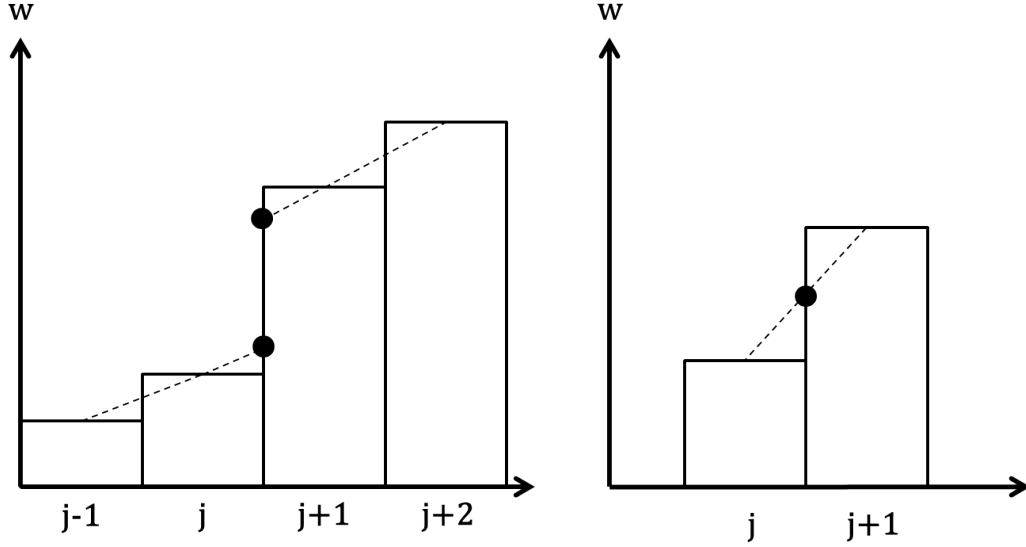


Figure 4: Schemes of the upwind (left) and centered (right) slope evaluation method.

with

$$\Delta_{j+\frac{1}{2}} = w_{j+1} - w_j; \quad \Delta_{j-\frac{1}{2}} = w_j - w_{j-1}; \quad \Delta_{j+\frac{3}{2}} = w_{j+2} - w_{j+1} \quad (31)$$

The upwind formulation is obtained with $\kappa = -1$, a centered formulation (2nd-Order) is obtained with $\kappa = 1$ and a third-order upwind biased (denoted as UB) formulation is obtained with $\kappa = -\frac{1}{3}$ [53].

3.3.2. Slope limiters

The extension of the spatial accuracy of the numerical scheme can lead to the apparition of spurious oscillations in the presence of high gradients. To avoid these numerical instabilities degrading the robustness of the computation, the slopes presented in the previous section have to be limited. In this study three MUSCL strategies are used and mixed as described in the next section. The most dissipative strategy (called Minmod) consists in the use of a centered formulation ($\kappa = 1$) combined with the Minmod limiter [55] Γ :

$$\begin{cases} w_{j+\frac{1}{2}}^L = w_j + \frac{1}{2}\Gamma(\Delta_{j+\frac{1}{2}}, \Delta_{j-\frac{1}{2}}) \\ w_{j+\frac{1}{2}}^R = w_{j+1} - \frac{1}{2}\Gamma(\Delta_{j+\frac{1}{2}}, \Delta_{j-\frac{1}{2}}) \end{cases} \quad (32)$$

with

$$\text{Minmod} : \Gamma(a, b) = \text{sign}(a) \max(0, \min(|a|, \text{sign}(a)b)) \quad (33)$$

The Minmod limiter thus selects the smallest slope in monovariant zones and reduces to first order accuracy around local extrema. The less dissipative strategy is to use the $\kappa = -1/3$ slope reconstruction without limiter, namely the third-order Upwind Biased formulation (called UB). Finally, we also use a limited version of the UB

200 formulation thanks to a Koren-type limiter $K(r)$ presented in [56] :

$$\begin{cases} w_{j+\frac{1}{2}}^L = w_j + K\left(\frac{\Delta_{j+\frac{1}{2}}}{\Delta_{j-\frac{1}{2}}}\right) \left[\frac{1-\kappa}{4} \Delta_{j-\frac{1}{2}} + \frac{1+\kappa}{4} \Delta_{j+\frac{1}{2}} \right] \\ w_{j+\frac{1}{2}}^R = w_{j+1} - K\left(\frac{\Delta_{j+\frac{3}{2}}}{\Delta_{j+\frac{1}{2}}}\right) \left[\frac{1+\kappa}{4} \Delta_{j+\frac{1}{2}} - \frac{1-\kappa}{4} \Delta_{j+\frac{3}{2}} \right] \end{cases} \quad (34)$$

With $\kappa = -\frac{1}{3}$ and:

$$\text{Koren} : K(r) = \frac{3r + \epsilon_2}{1 + r + r^2 + \epsilon_2}, \quad \epsilon_2 = 1e^{-32} \quad (35)$$

As showed in Fig.5, this formulation (called Koren here) is close to the third-order Upwind Biased one (UB) when $K(r) \approx 1$, that is to say when the ratio r between the right and left slopes is around 1 and is limited otherwise $K(r) < 1$.

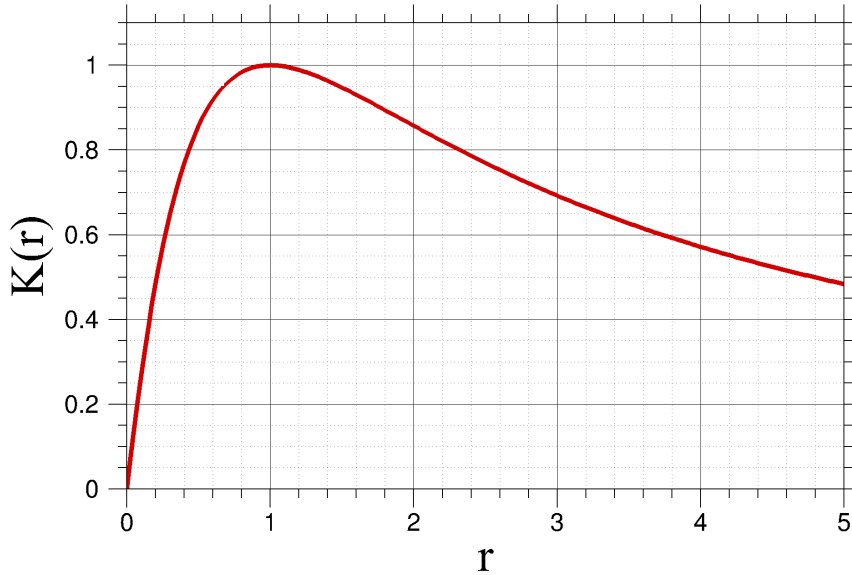


Figure 5: Variation of the Koren limiter.

205 3.3.3. Hybrid MUSCL formulation

As described in Sec. 1.3, the good numerical accuracy showed in [12] [17] is obtained thanks to the combination of a low dissipation AUSM+(P) scheme and a UB MUSCL reconstruction. The hybrid scheme formulation presented above enables to retain the accuracy of the low dissipation AUSM+(P) in desired regions and the selection of the MUSCL reconstruction method is discussed in the following. Indeed, it is shown in [28] that the AUSM+ scheme, which is used for the shock capturing part of the hybrid scheme, enables to compute strong shock tube cases with a Minmod or a Koren reconstruction but not with the UB reconstruction. We thus propose here a hybrid MUSCL reconstruction strategy to complete the hybrid numerical scheme formulation. At a cell interface the left and right states are computed as:

$$\Psi_{L,R} = (1 - \beta') \Psi_{L,R}^{(3)} + \beta' \Psi_{L,R}^{(2)} \quad (36)$$

With $\Psi_{L,R}^{(2)}$ being the state obtained with a 2nd-order MUSCL reconstruction (here Minmod) and $\Psi_{L,R}^{(3)}$ being the state obtained with a 3rd-order MUSCL reconstruction (here Koren or UB). β' is equal to β (see Eq.27) but can be forced to 1 in desired zones.

Based on this framework we have used two different reconstruction strategies for computations with jet. First, a Koren/Minmod strategy is tested with a Koren reconstruction for $\Psi_{L,R}^{(3)}$, a Minmod reconstruction for $\Psi_{L,R}^{(2)}$ and $\beta' = \beta$. Second a UB/Minmod strategy is assessed with a 3rd-Order upwind biased (UB) reconstruction for $\Psi_{L,R}^{(3)}$, a Minmod reconstruction for $\Psi_{L,R}^{(2)}$, $\beta' = \beta$ out of the jet zones and $\beta' = 1$ in the jet zones. Indeed if β' is not forced to 1 in jet zones, that is to say if a full Minmod reconstruction is not used, the UB/Minmod reconstruction is not robust enough and the computation diverges.

4. Test case

The test case configuration is an axisymmetric afterbody studied experimentally by Depres et al. ([1], [2]) in ONERA's S3Ch wind tunnel. Experiments were performed with and without a cold air propulsive jet.

4.1. Experimental setup

As shown in Fig.6a the model consists in an axisymmetric blunt body with a diameter $D=2R$ equal to 100 mm and a 60mm-long extension with a smaller diameter $d=2r$ equal to 40 mm. The ratios $\frac{L}{D} = 0.6$ and $\frac{d}{D} = 0.4$ are representative of current space launcher designs [57] [5].

The free stream Mach number is set to 0.702 in the wind tunnel and the nozzle pressure ratio ($\text{NPR} = \frac{P_{t_j}}{P_0}$) of total jet pressure (P_{t_j}) over freestream pressure (P_0) is 34.2, which corresponds to an adapted jet i.e.(exit jet pressure close to the external pressure). The Reynolds number of the external flow, based on the forebody diameter, is Re_D is 1.2×10^6 .

4.2. Meshing

The mesh is presented in Fig.(6b). In coherence with experimental measurements, the computed forebody length was chosen to ensure a ratio $\frac{\delta}{D} = 0.2$ between the external boundary layer thickness δ and the forebody diameter. 40 points are clustered in this boundary layer and the $\Delta y^+ = 1$ condition is satisfied. In Fig.7, one can verify that the thickness of the computed boundary layer compares well with experimental measurements for different azimuthal angles. The multi-block structured meshes used contain 12.5M cells for the no-jet case and 16.2M cells for the case with jet (Fig. 6c). 240 points are distributed in the azimuthal direction resulting in a discretization $\Delta\theta = 1.5^\circ$. Besides, an O-H grid topology is adopted to avoid a singularity on the axes.

4.3. Numerical setup

Ten different computations have been performed for this study to compare the several methodologies described in the previous sections. For each of the configurations (with and without jet), four different ZDES computations and a RANS AUSM+ computation have been run, as summarized in table 3. ZDES computations were run with 5 sub-iterations. First, we let the flow develop for 200 ms ($\approx 100 \times Ts$ with Ts the vortex shedding period) to avoid

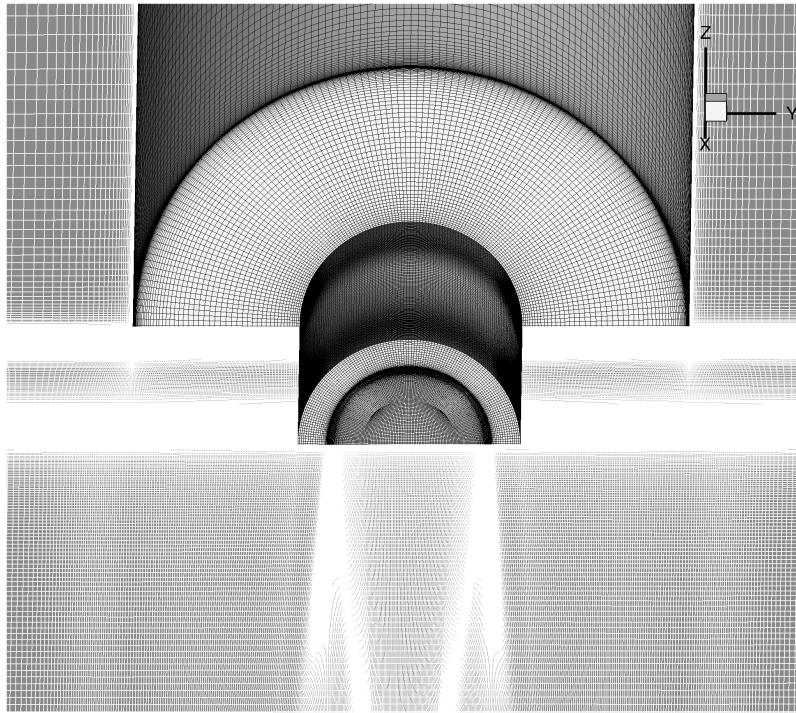
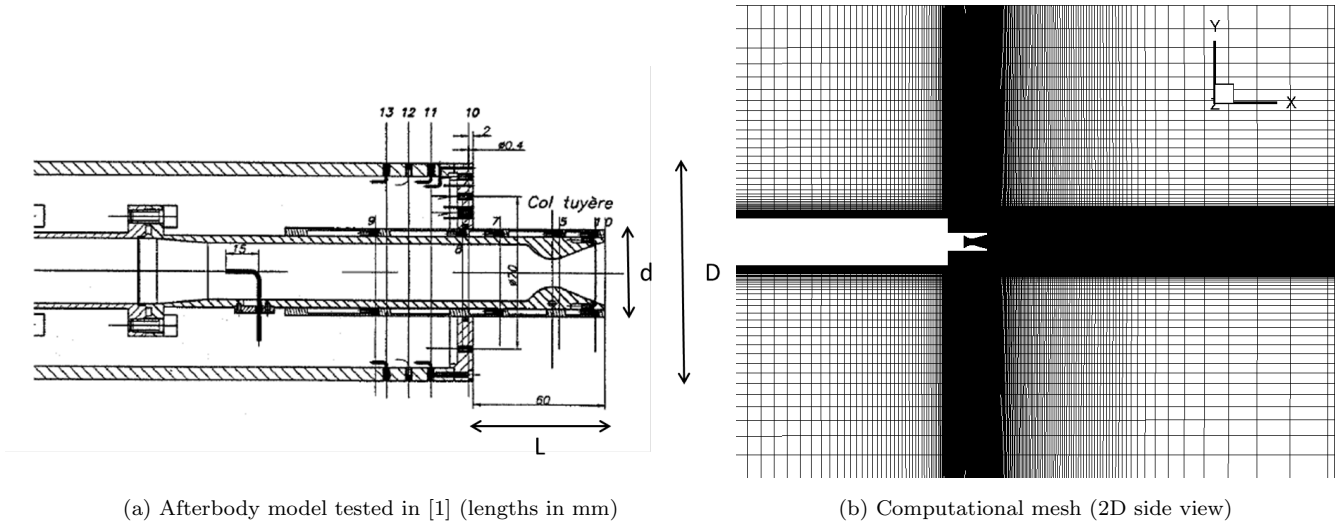


Figure 6: Test case setup

transitory effects and statistical properties are then computed on the fly for 200 ms as well.

240

The various computational configurations listed in Tab.3 enable a gradual assessment from the current numerical standards for a generic transonic afterbody geometry without jet (NJ1) to our proposition for a numerical framework adapted to complex space launcher geometries with propulsive jet (J4). During this process, comparing NJ1 vs NJ3 enables to evaluate the performance of the hybrid scheme (used in NJ3) compared to the LD AUSM+(P) scheme (used in NJ1) on a configuration without shocks. Then, the performance of the hybrid scheme for cases

245

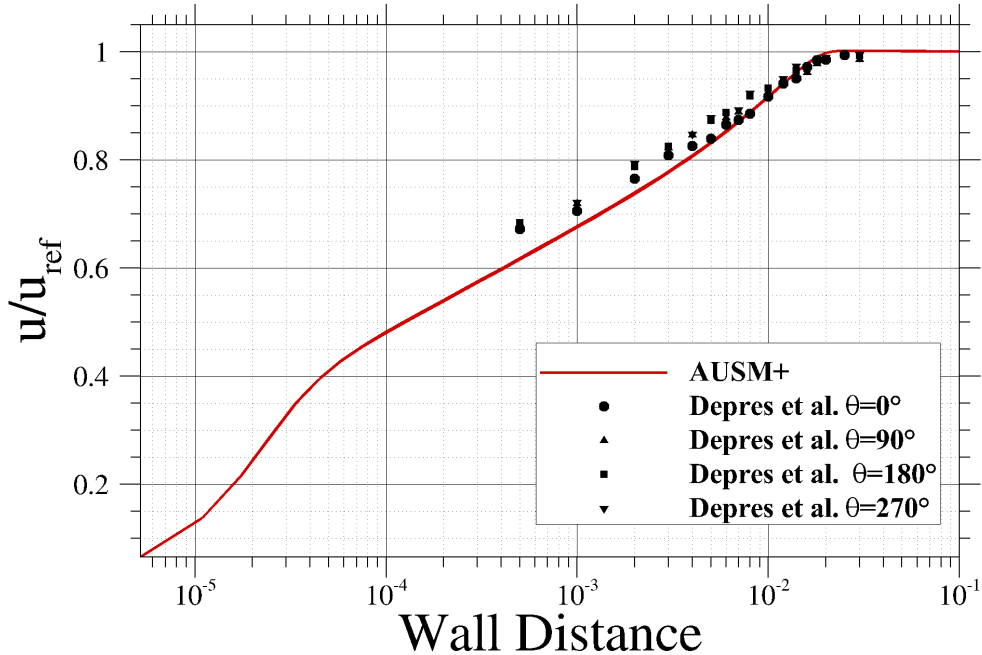


Figure 7: Boundary layer profile on the forebody at the station $X/D=-2.45$

with propulsive jet is tested with all jet computations [J1-J2-J3-J4] and the accuracy of the different MUSCL reconstruction methods is judged thanks to the comparisons [NJ3 vs NJ4; J1 vs J3 and J2 vs J4]. Finally, the comparisons [NJ1 vs NJ2; J1 vs J2; J3 vs J4] enable to assess the performance of the latest development of the automatic mode of ZDES (ZDES mode 2 (2020) [35]) in comparison to the mode 1.

| Without Jet (NJ) | | | |
|------------------|-----------|------------------|--|
| CODE | ZDES mode | Numerical Scheme | MUSCL Reconstruction |
| RANS-NJ | 0 | AUSM+ | Minmod |
| NJ1 | 1 | LD AUSM+(P) | UB |
| NJ2 | 2 | LD AUSM+(P) | UB |
| NJ3 | 1 | Hybrid | UB |
| NJ4 | 1 | Hybrid | Koren |
| With Jet (J) | | | |
| CODE | ZDES mode | Numerical Scheme | MUSCL Reconstruction |
| RANS-J | 0 | AUSM+ | Minmod |
| J1 | 1 | Hybrid | Hybrid Minmod/UB and Minmod in the jet |
| J2 | 2 | Hybrid | Hybrid Minmod/UB and Minmod in the jet |
| J3 | 1 | Hybrid | Hybrid Minmod/Koren |
| J4 | 2 | Hybrid | Hybrid Minmod/Koren |

Table 3: List of computational setups used. UB= Upwind Biased ($\kappa = -\frac{1}{3}$ in Eq.30), LD= Low Dissipative version [50].

250 5. Results

We present here the results obtained for the afterbody computations with and without jet. In addition to the physical description of the flow, this section will provide an evaluation of the developed numerical workflow. Indeed, numerical data are compared with both experimental measurements and previous numerical studies following the aforementioned nomenclature for validation of simulation techniques [3] (see Tab 1).

255 5.1. Flow topology

5.1.1. Instantaneous visualisations

The salient features of the instantaneous flow described in [12] are evidenced in Fig.8 and Fig.9 by plotting an iso-surface of the Q-criterion. The roll-up of the mixing layer induces the formation of azimuthal coherent structures which are disrupted by azimuthal instabilities and progressively bent in the flow direction to form hairpin vortices as they are convected near the reattachment point. Passed the reattachment we mainly observe longitudinal eddies. Note that almost no differences can be seen between NJ1 and NJ4 computations showing that the desired properties of the proposed hybrid scheme in vortical regions are achieved. A sliced view of the flow provided in Fig.10 confirms the global similarity between the two computations but enables to observe that the NJ1 computation resolves more turbulent structures close to the base. In other words, the use of the hybrid scheme and the Koren limiter induces a minor increase of the numerical dissipation in smooth regions. The presence of the jet tends to amplify the stretching and the alignment of the structures with the flow direction after the extension due to a higher entrainment effect. Furthermore, for the case with jet, the J3 computation (Koren/Minmod) allows to advect more structures from the recirculation area into the jet area than the J1 computation (Minmod in the jet area). This observation is confirmed in Fig.10. The J3/J4 hybrid MUSCL strategy is thus both less dissipative in the jet area and easier to use than the J1/J2 MUSCL strategy. Indeed, the decision load of the user is very low for computation J4 which is automatic on both numerical and turbulence treatment aspects. Fig.10 also displays the strong normal shock structure of the jet which is classically the source of numerical difficulties. Overall, the present ZDES computations using the hybrid scheme are robust and permit a noticeable improvement in scale resolving compared to results obtained in [10] using Roe's scheme on a similar mesh.

275 5.1.2. Mean flow topology

The main properties of the mean velocity fields are shown in Fig.11. Let us be reminded that for a short extension length, the flow does not reattach on the solid part of the rear body (see Fig.1). No PIV measurements were made during Depres' experiments [1] but PIV results from two other experimental campaigns [22][24] can be used here for the analysis. The test conditions during these campaigns, [22] ($D=50$ mm, $d/D=0.34$, $L/D=0.6$, $M_\infty = 0.76$, model held by a strut, tests with and without jet) and [24] ($D=66.7$ mm, $d/D=0.4$, $L/D=0.6$, $M_\infty = 0.8$, tests with jet), were close but nevertheless not equivalent to the present cases.

We observe in Fig.12 that the presence of the jet causes both a shortening of the recirculation bubble and an increase of the backflow velocity around the extension. This effect is predicted by both RANS and ZDES computations. More precisely, in the absence of the jet, ZDES computations predict a longer recirculation bubble ($\frac{L_r}{D} \approx 1.5$) than the RANS computation ($\frac{L_r}{D} \approx 1.16$). For this particular flow characteristic, the RANS predictions appear closer

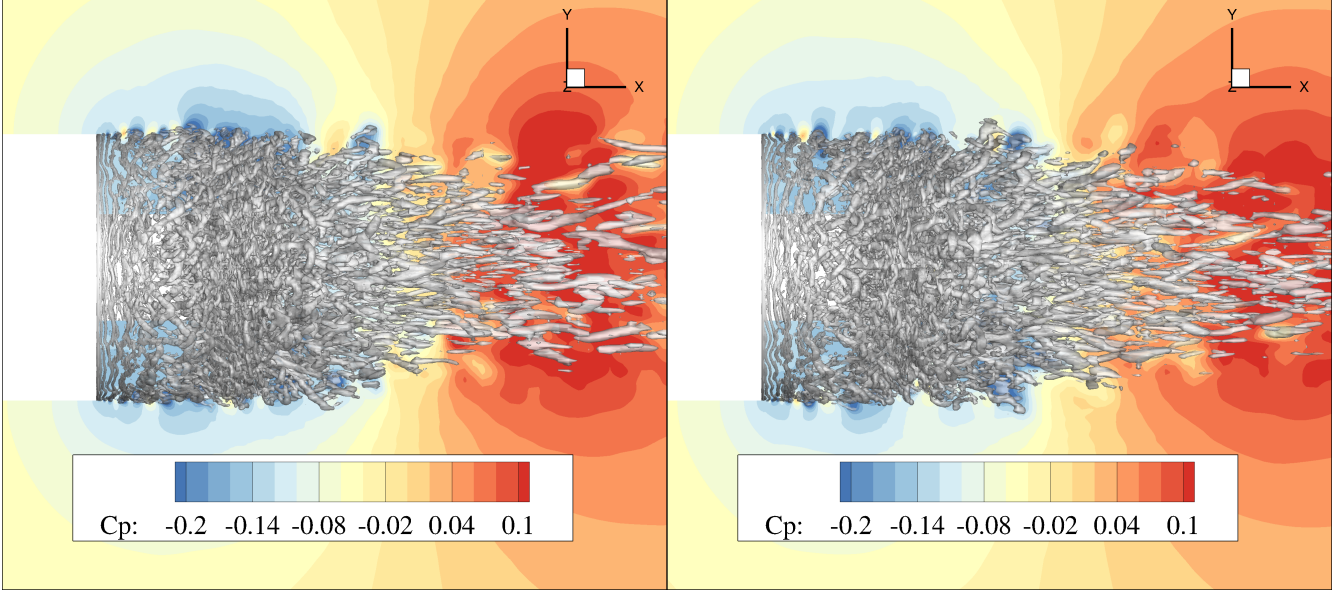


Figure 8: Instantaneous flow visualization of the NJ1 (left) and NJ4 (right) computations for the case without jet. Iso-surfaces of Q criterion ($Q \cdot D^2 / U_{ref}^2 = 50$) and iso-contours of pressure coefficient. (See Tab. 3 for computation details)

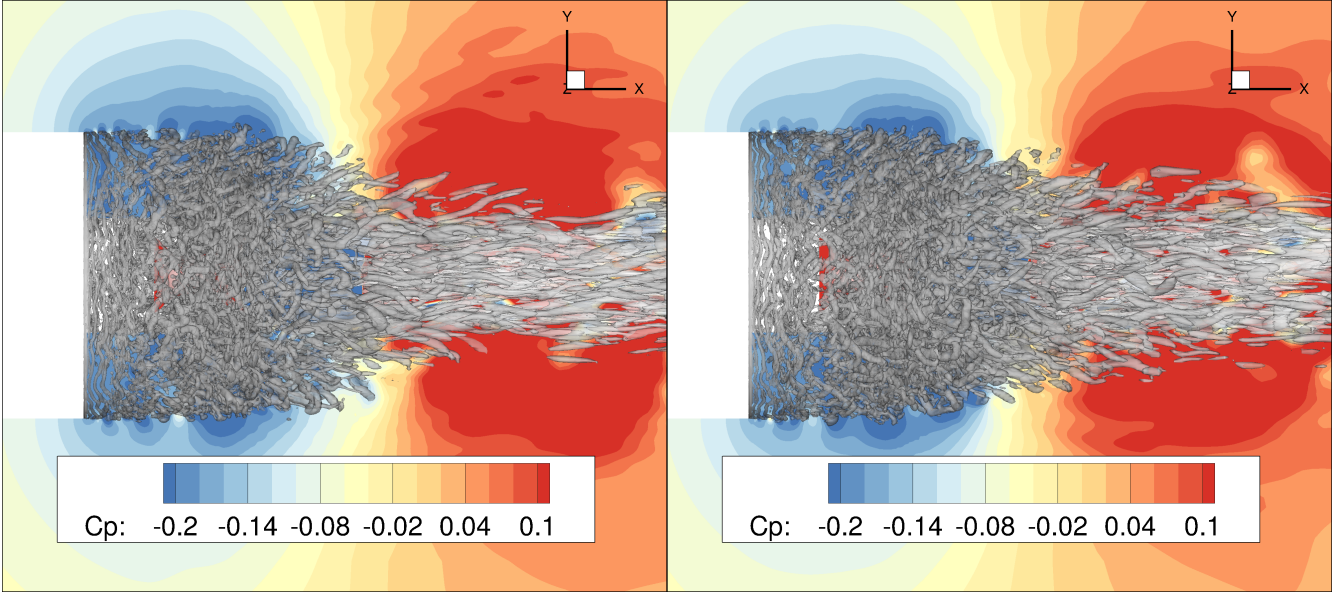
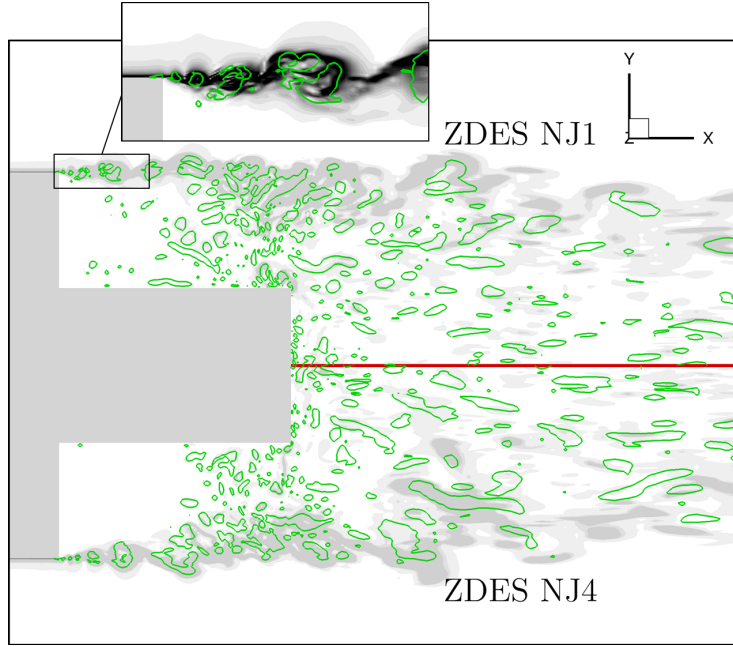
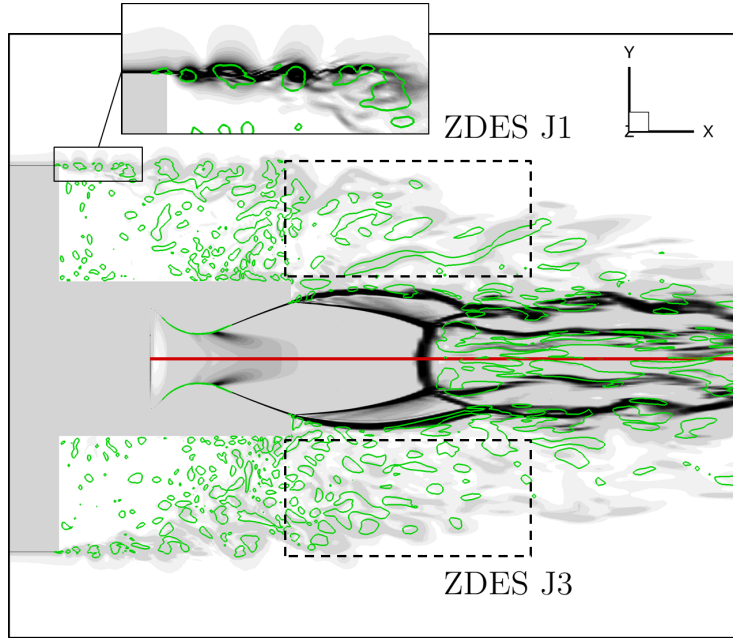


Figure 9: Instantaneous flow visualization of the J1 (left) and J3 (right) computations for the case with jet. Iso-surfaces of Q criterion ($Q \cdot D^2 / U_{ref}^2 = 50$) and iso-contours of pressure coefficient. (See Tab. 3 for computation details)

to PIV results obtained on a strut-mounted model [22] ($\frac{L_r}{D} \approx 1.15$). In the case with jet, $\frac{L_r}{D} \approx 1.05$ with ZDES, $\frac{L_r}{D} \approx 0.75$ with RANS where experimental PIV results on similar cases found $\frac{L_r}{D} \approx 0.95$ [24][22]. Focusing on the backflow velocity distribution inside the recirculation bubble, ZDES results appear closer to PIV measurements than RANS ones which display an overestimation of the backflow velocity along the extension. In the absence of the jet, ZDES computations predict the occurrence of a small reattachment bubble (with $\frac{u}{U_{ref}} \approx 0.05$) at the end of the extension. This observation can be related to PIV results [58] showing that the probability of reversed flow



(a)



(b)

Figure 10: Instantaneous flow visualization with pseudo numerical schlieren (scales of $\frac{\nabla \rho}{\rho}$ contours adapted in the zoomed area) and iso-lines of Q criterion ($Q \times D^2 / U_{ref}^2 = 30$)(green). (a) NJ1 (top) and NJ4 (bottom) computations for the case without jet. (b) J1 (top) and J3 (bottom) computations for the case with jet. (See Tab. 3 for computation details)

($P(u < 0)$) decreases from $P \geq 0.8$ in the center of the recirculation to $P \leq 0.6$ near the end of the extension.

Overall, Fig.12 (without jet) and Fig.13 (with jet) show that the different ZDES formulations (namely mode 1 and mode 2) used provide very similar flow topologies. Let us be reminded that the mode 2 formulation is fully automatic from the user's side.

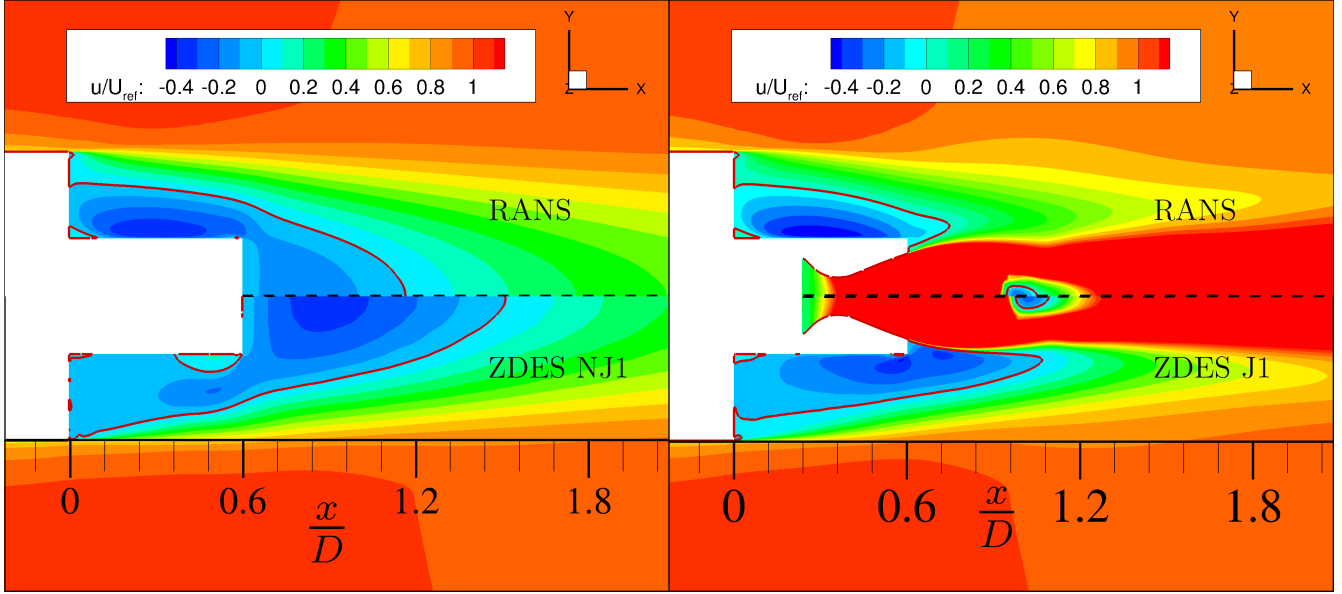


Figure 11: Mean flow topology for RANS and ZDES NJ1 for the case without jet (left) and RANS and NJ1 for the case with jet (right). — isoline $\frac{u}{U_{ref}}=0$. (See Tab. 3 for computation details)

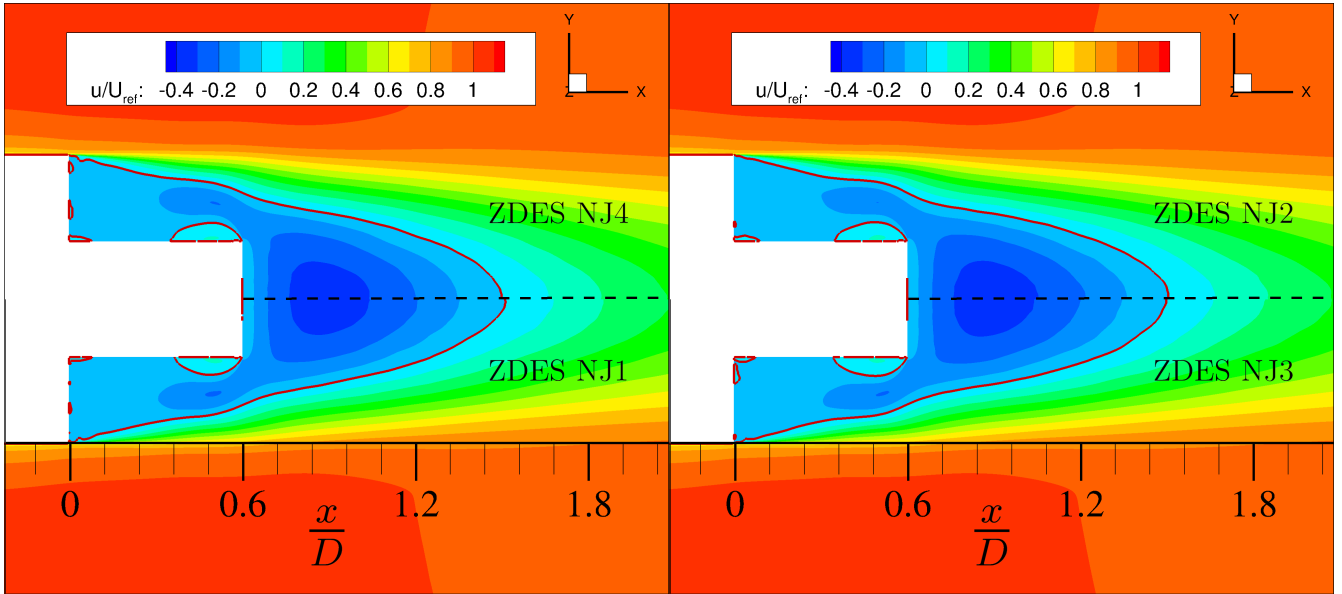


Figure 12: Mean flow topology with the four ZDES set-ups for the case without jet. — isoline $\frac{u}{U_{ref}}=0$. (See Tab. 3 for computation details)

5.2. Statistical properties of the wall pressure field

The distribution of mean (C_p) and fluctuating ($C_{p_{rms}}$) pressure coefficients on the base and on the extension are discussed here. Fig.14 indicates an important decrease in base pressure (i.e. an increase in base drag) due the presence of the jet as shown by both experimental and numerical results. Indeed, ZDES calculations for the jet-off case exhibit a flat C_p profile with $-0.138 \leq C_p \leq -0.135$ illustrating the good agreement with experimental results in which $-0.131 \leq C_p \leq -0.124$. However, when jet is on, the C_p levels fall to $-0.18 \geq C_p \geq -0.185$ according

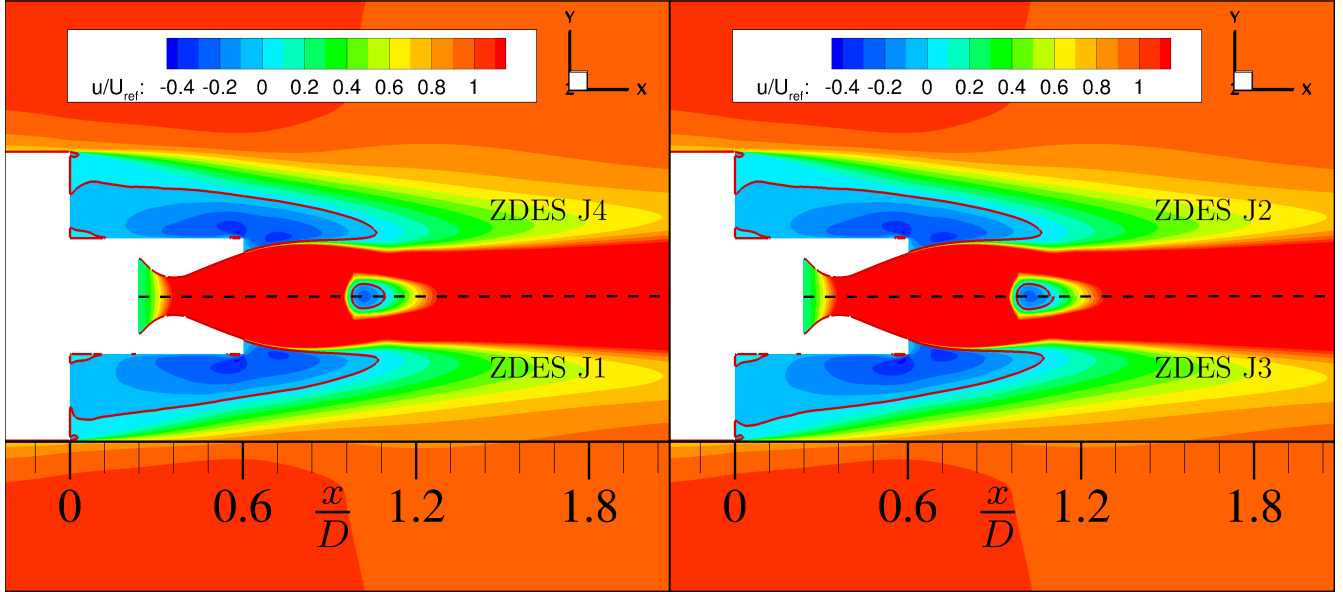


Figure 13: Mean flow topology with the four ZDES set-ups for the case with jet. — isoline $\frac{u}{U_{ref}}=0$. (See Tab. 3 for computation details)

to ZDES computations and $-0.195 \geq C_p \geq -0.21$ on wind tunnel measurements. The observed discrepancy in this case points out that the aspiration effect of the jet is underestimated numerically. RANS results present major discrepancies both in mean pressure levels and on their radial variation.

305 The pressure drop induced by the jet is even more important when looking at the longitudinal variation of C_p on the extension presented in Fig.15. One can notice a global improvement on pressure level predictions with current ZDES computations compared to [10] both with and without the jet. Present RANS results are very far from being in agreement with the experimental data. This is consistent with the overestimation of the recirculation velocity previously described. Similar disparities for classical RANS models have been reported in [26] [59].

310 Focusing on the distribution of pressure fluctuations along the extension (Fig.16), we observe a continuous increase in the intensity of the fluctuations in the x-direction both with and without the jet. Furthermore, as described in the literature, the overall Cp_{rms} levels are noticeably higher in the presence of the jet, especially near the end of the extension. The fluctuation levels are slightly underestimated by ZDES computations near the base but their rise in the second half of the extension is well captured. Let us be reminded that the incoming attached
 315 boundary layer is treated in URANS within mode 1 and mode 2 of ZDES. The assessment of incoming fluctuations inherited from the boundary layer is beyond the scope of this study but could be envisaged in the future within mode 3 of ZDES [60].

For mean values and second order statistics of wall pressure, the displayed results show that the different ZDES computations provide results very close to each other. For the case without jet, a minor discrepancy is the behaviour
 320 of the mode 2 computation (NJ2) at the end of the extension. Indeed, compared to the other mode 1 results, it slightly underestimates the Cp_{rms} levels (Fig.16) and overestimates the mean pressure level (Fig.15) for $x/D \geq 0.45$. This difference can be attributed to the deactivation of wall functions (used in RANS and mode 2 of the ZDES) when using the mode 1 of the ZDES (see [29]), which induces a different treatment of the small reattachment

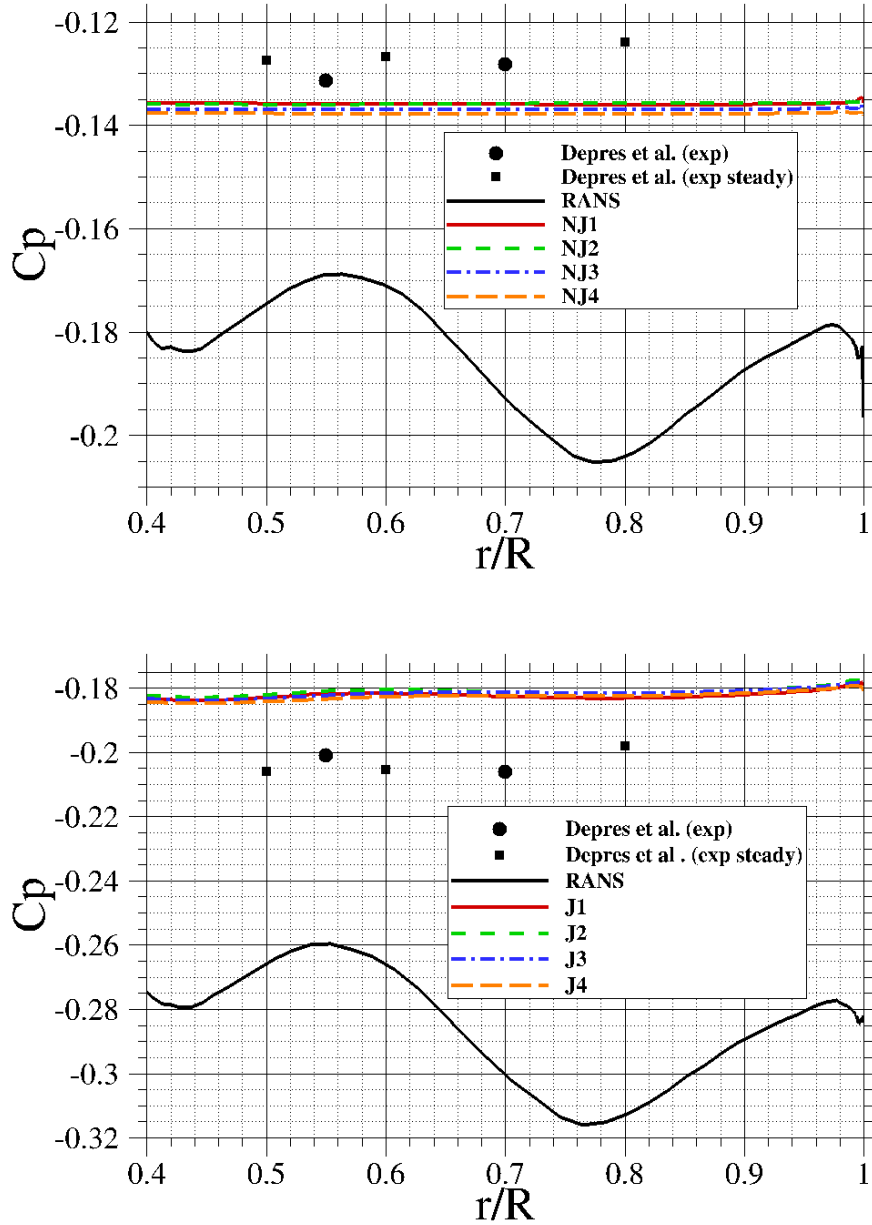


Figure 14: Distribution of the pressure coefficient on the base without jet (top) and with jet (bottom). (See Tab. 3 for computation details)

bubble observed at the end of the extension on Fig.12. In the presence of the jet, one can observe that the two
 325 computations using the Koren/Minmod reconstruction (J3 and J4) tends to slightly underestimate the level of
 fluctuations (Fig.16) in comparison with the UB/Minmod computations (J1, J2). This can be attributed to the
 extra dissipation induced by the use of the Koren limiter compared to the unlimited Upwind Biased slope in the base
 area as seen in Fig.10. However, the two computations (J3 and J4) using a hybrid $\Psi^{(3)}/\Psi^{(2)}$ limiter formulation
 (see Sect.3.3.3) in the jet area found a lower pressure coefficient near the jet compared to the two using a $\Psi^{(2)}$
 330 limiter in this area (J1; J2). In this zone, the formulation used in (J3; J4) is the less dissipative and provides an
 increase of the jet aspiration effect. This effect on pressure levels is nevertheless limited to the area near the jet

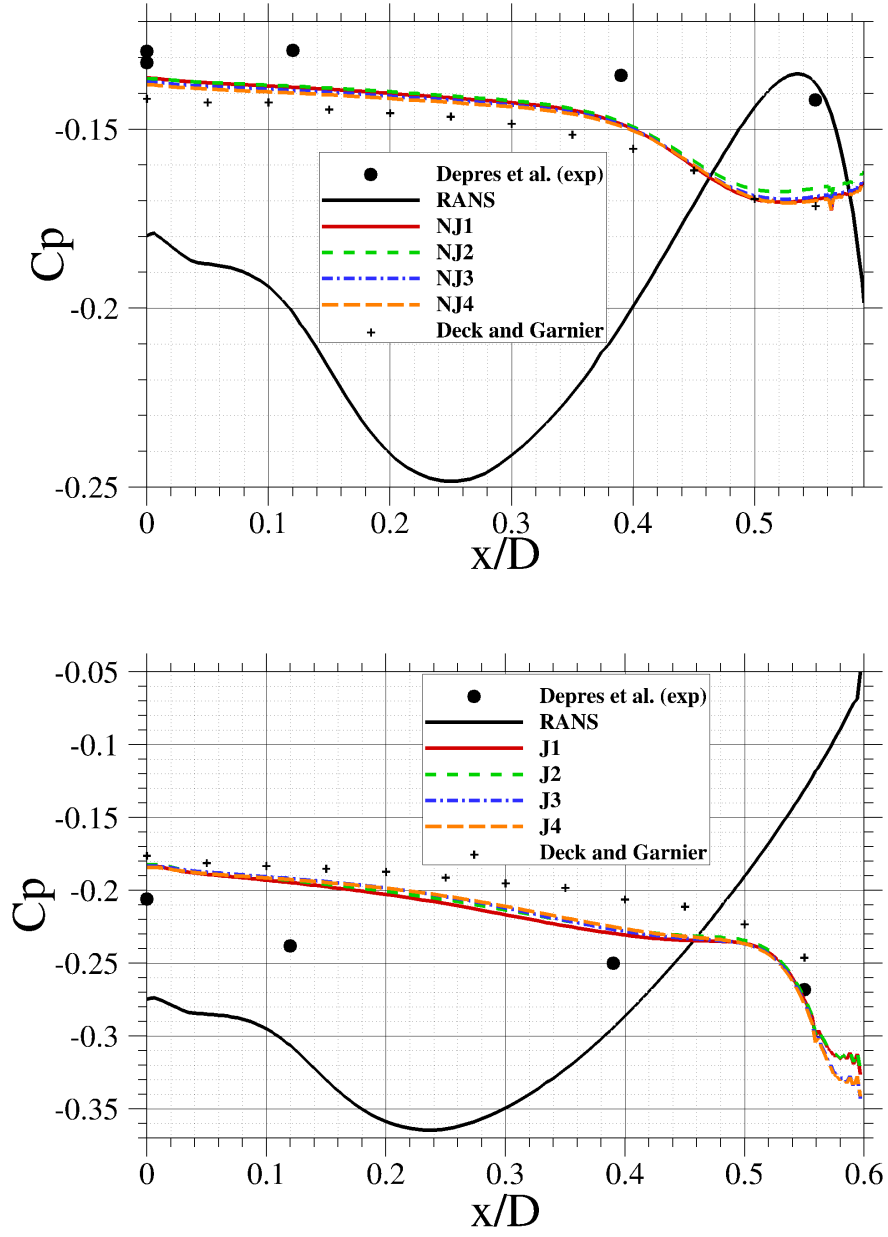


Figure 15: Distribution of the pressure coefficient on the extension without jet (top) and with jet (bottom). (See Tab. 3 for computation details)

and does not provide a decrease on base pressure levels.

5.3. Spectral analysis

To study more deeply the dynamic behaviour of the base flow, one can examine the spectral distribution of the pressure fluctuations mentioned above to determine characteristic frequencies. Indeed, $Cp_{rms} = \frac{p_{rms}}{q_\infty}$ with $q_\infty^2 = \frac{1}{2}\gamma p_\infty M_\infty^2$ the dynamic pressure and one can express p_{rms} values as:

$$p_{rms} = \int_0^\infty G(f)d(f) = \int_0^\infty G(St_D)d(St_D) \quad (37)$$

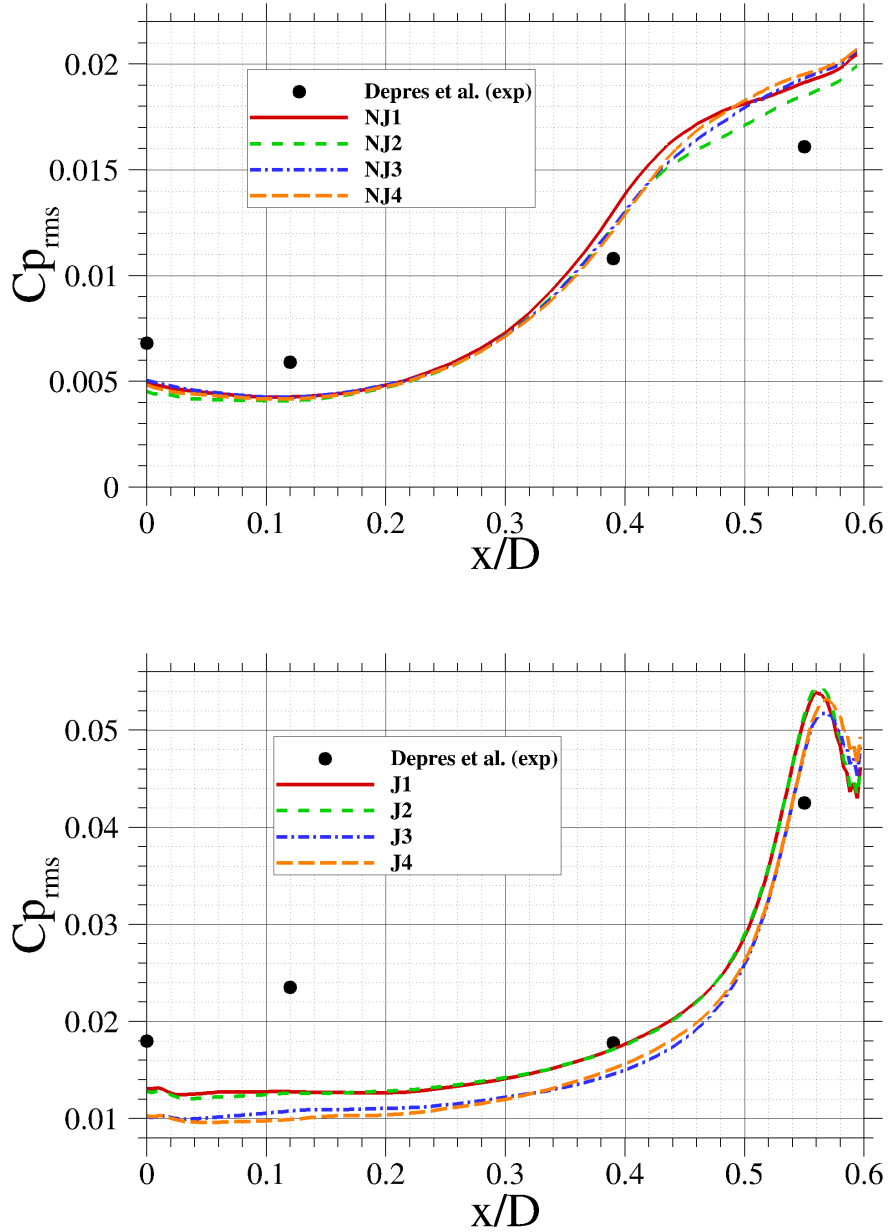


Figure 16: Distribution of the pressure fluctuations on the extension without jet (top) and with jet (bottom). (See Tab. 3 for computation details)

With G the power spectral density (PSD) of the pressure signal, computed here thanks to a Welch's periodogram method applied on experimental (1.6 s) and numerical (0.2 s) pressure signals. We will study the power spectral density of fluctuations near the end of the extension ($x/D=0.55$), where pressure fluctuations are the strongest, and on the base of the afterbody ($r/R=0.7$). The PSD is normalized and the plots show the frequency distribution of $G(f) \cdot \frac{U_\infty}{Dq_\infty^2}$.

Fig.17 shows the pressure spectra near the end of the extension ($x/D=0.55$) for the plume-off and plume-on cases. In both cases, we observe a sharp peak around $St_D \approx 0.2$, as discussed in Sec.1.2.1, this contribution is usually attributed to the vortex shedding phenomenon [1] [12]. This peak is although of less importance in the overall

pressure fluctuations in the presence of the jet as the contribution of low frequency fluctuations $St_D \leq 0.1$ is superior than for the no-jet case. Overall, the ZDES computations reproduce well the spectral distribution of fluctuations found experimentally. The secondary contributions found experimentally for the plume-off case namely a small peak at $St_D \approx 0.26$ and a broadband contribution between $St_D \approx 0.3$ and $St_D \approx 0.6$ are only partially captured numerically as we observe a plateau between $St_D \approx 0.25$ and $St_D \approx 0.4$. Both the smaller duration of the pressure signal and the absence of the smallest turbulent scales may explain this differences.

Fig.18 shows the pressure power spectral density on the base of the afterbody. If the presence of a peak around $St_D \approx 0.2$ is found both experimentally and numerically for the case without jet, showing that the vortex shedding phenomenon also affects the pressure fluctuations on the base, no clear sign of this contribution is found in the presence of the jet. In both cases, the main source of pressure fluctuations is a low frequency range $St_D \leq 0.1$ as shown in the broadband spectra in Fig.18. Such a contribution is found numerically, even though it is underestimated compared to the experiment. Indeed, as regards base pressure fluctuations, the level of fluctuations is underestimated by all ZDES computations. The smaller duration of the pressure signal and the absence of turbulent fluctuations within the incoming boundary layer can again partially explain those discrepancies but it is also worth noticing that the experimental probes ($r/R=0.7$) are located just under the delimitation of the recirculation bubble found numerically (Fig.13). The discrepancies observed in pressure fluctuations on the base could thus be partially caused by a different relative position between the probe and the recirculation bubble in the experiment.

Apart from the slight underestimations of the overall fluctuation level found in Fig.16 with the J3 and J4 computations and again noticeable in Fig.17 and Fig.18, the different ZDES computations again display very close results. This indicates that the automatic shock-capturing formulation proposed (J4) is able to retain most of the shock-free reference framework (NJ1) accuracy. This is further confirmed by the two-point spectral analysis displayed below.

5.4. Two-point analysis

To study the spatial organization of the flow at the previously highlighted frequencies, the azimuthal coherence of two pressure sensors $p_1(r, x, \phi_1)$ and $p_2(r, x, \phi_2)$ located in a plane normal to the inflow at a constant position x/D and a constant radius r/R can be considered. Assuming the hypothesis of an homogeneous flow, i.e. without any preferred angle of reference ϕ_1 , the complex coherence function may be expressed as:

$$C(f, r, x, \Delta\phi) = (C_r + jC_i)(f, r, x, \Delta\phi) = \frac{S_{12}(f, r, x, \Delta\phi)}{\sqrt{S_1(f, r, x, \Delta\phi)S_2(f, r, x, \Delta\phi)}} \quad (38)$$

where $j = \sqrt{-1}$, and C_r and C_i are the real and imaginary part of the cross-spectral density function S_{12} and $\Delta\phi = \phi_1 - \phi_2$. Assuming that the disturbances do not exhibit any particular direction of propagation, one has $S_{12}(\Delta\phi) = S_{12}(-\Delta\phi)$. Besides, the hypothesis of isotropy yields $C_i = 0$. Consequently, the C_r function is 2π -periodic with respect to $\Delta\phi$ and can, thanks to a Fourier transform in azimuthal modes, be expressed as:

$$C_r(f, \Delta\phi) = \sum_{m=0}^{\infty} C_{r,m}(f) \cos(m\Delta\phi). \quad (39)$$

$C_{r,m}$ represents the percentage of the fluctuating energy at frequency f relative to the azimuthal mode m since $\sum C_{r,m} = 1$. Let us be reminded that $m = 0$ and $m = 1$ modes are characterized by an inphase and antiphase

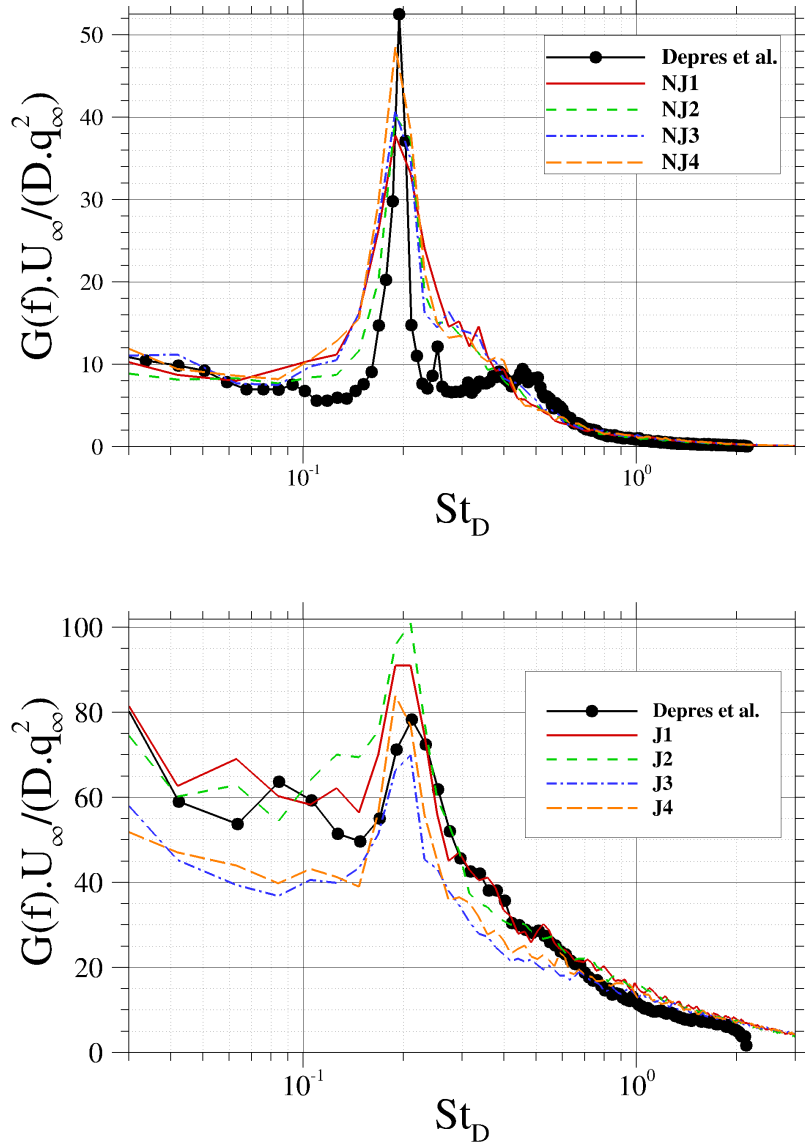


Figure 17: Power spectral density of the fluctuating pressure near the end of the extension ($x/D=0.55$) without jet (top) and with jet (bottom). (See Tab. 3 for computation details)

relationship of signals, respectively, recorded simultaneously at two diametrically opposed locations. An anti-symmetric pressure variation on the extension is the source of side-loads that may excite the structure [61].

Similar experimental behaviours can be witnessed at the end of the extension (Fig.19a;19c;19e) and on the base (Fig.19b;19d;19f) of the afterbody for the case without jet. The low frequency contributions (i.e. $St_D \leq 0.1$) to pressure fluctuations appear as a combination of symmetric and anti-symmetric motions whereas the $St_D \approx 0.2$ contribution is clearly linked to an anti-symmetric motion (see [12][25] for further discussion on the dynamics associated with $St_D \approx 0.2$), which can be the source of side-loads on the structure.

As shown in (Fig.20 (c)), in presence of the jet, the spatial organization of the pressure field around a unique anti-symmetric mode ($m=1$) is less obvious. In good agreement with experimental results, the ZDES computations predict that the predominance of the anti-symmetric motion at the vortex-shedding frequency is still noticeable on

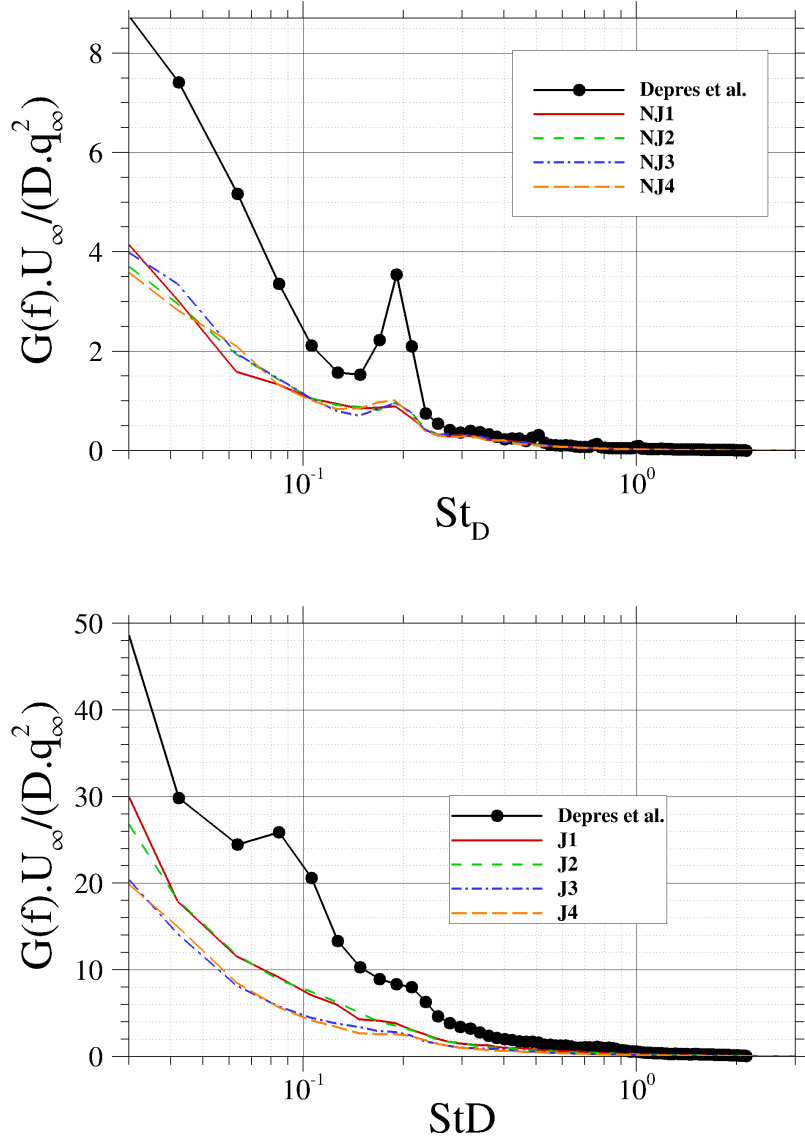
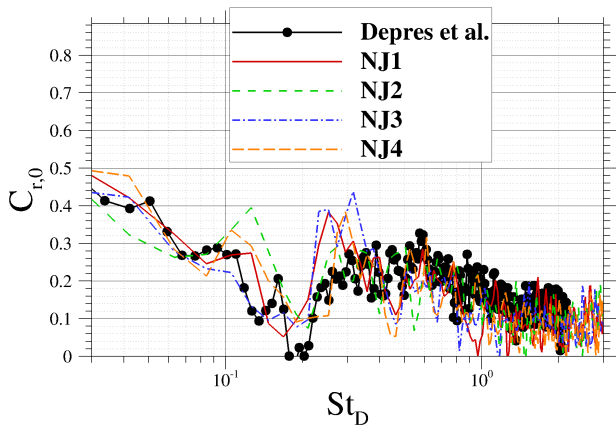


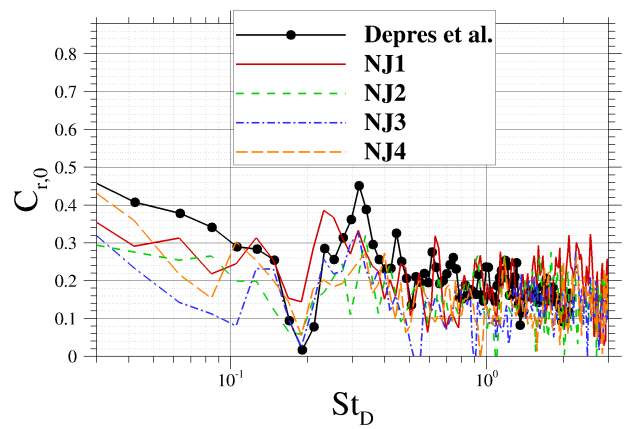
Figure 18: Power spectral density of the fluctuating pressure near the end of the base ($r/R=0.7$) without jet (top) and with jet (bottom). (See Tab. 3 for computation details)

the end of the extension ($C_{r,1}(St_D = 0.2) \approx 55\%$) but is less pronounced than in the case without jet ($C_{r,1}(St_D = 0.2) \approx 80\%$). The presence of the jet seems to have a stabilizing effect on the vortex shedding. The contributions of the first three azimuthal modes appear balanced for other frequencies. On the base, the observed low frequency contribution ($St_D \leq 0.1$) seems also dominated by an anti-symmetric motion (Fig.20 (d)). Here again, the results provided by the ZDES computations are close to each other and reproduce well the overall spatial behaviour observed experimentally. Overall, the presented results show that the proposed hybrid numerical strategy enabled to resolve well the turbulent fluctuations of the base flow while capturing the strong normal shock structure of the jet.

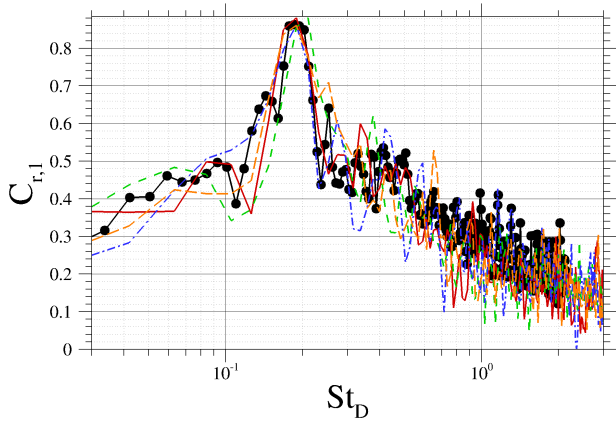
385



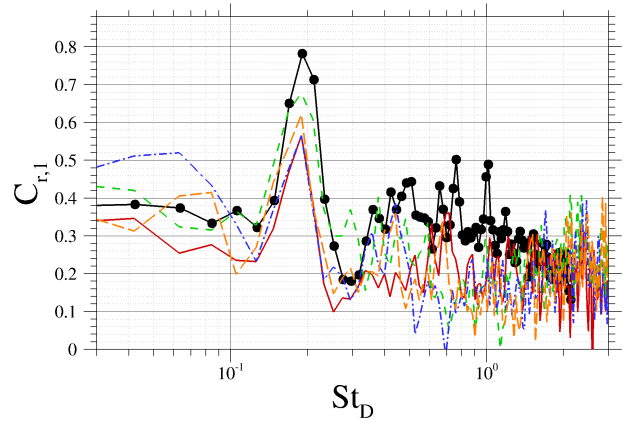
(a)



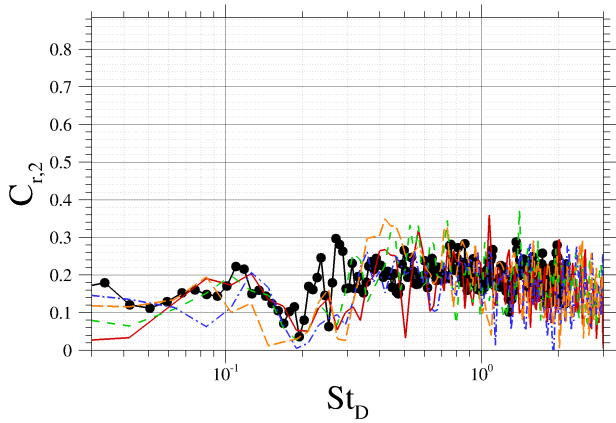
(b)



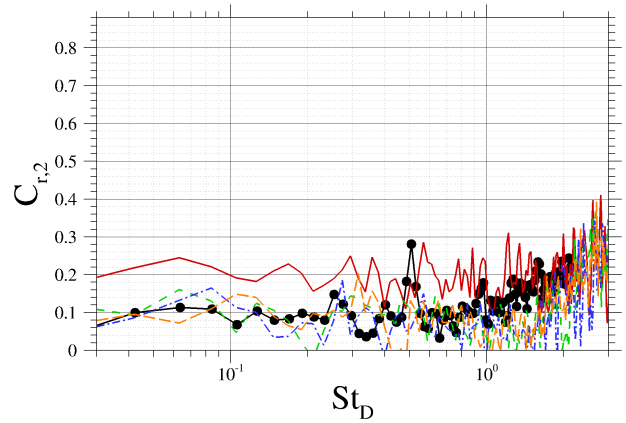
(c)



(d)

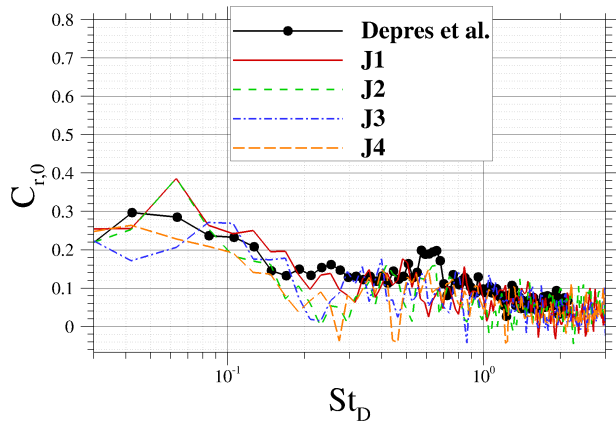


(e)

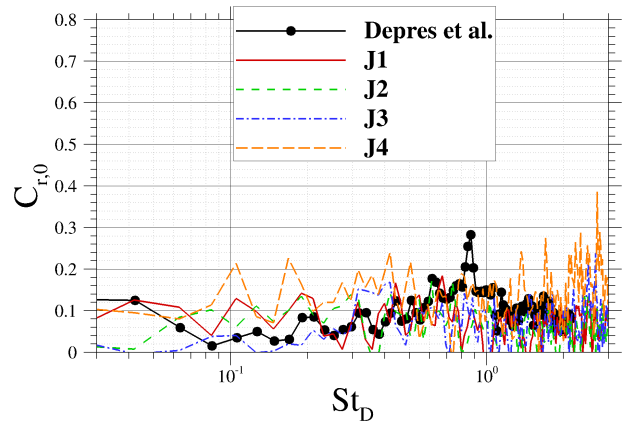


(f)

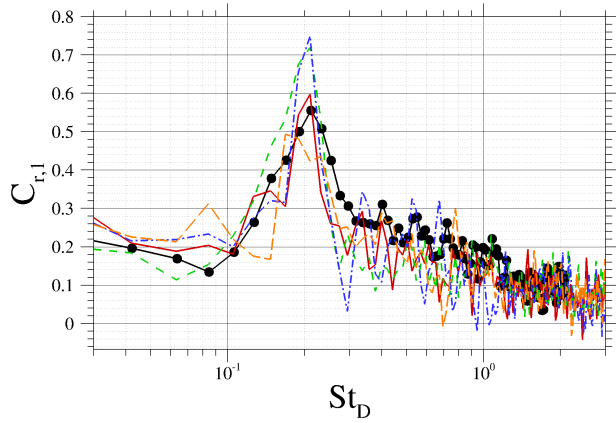
Figure 19: Spectra of the first 3 azimuthal modes for the case without jet. (a)-(c)-(e) on the extension ($x/D=0.55$). (b)-(d)-(f) on the base ($r/R=0.7$). (See Tab. 3 for computation details)



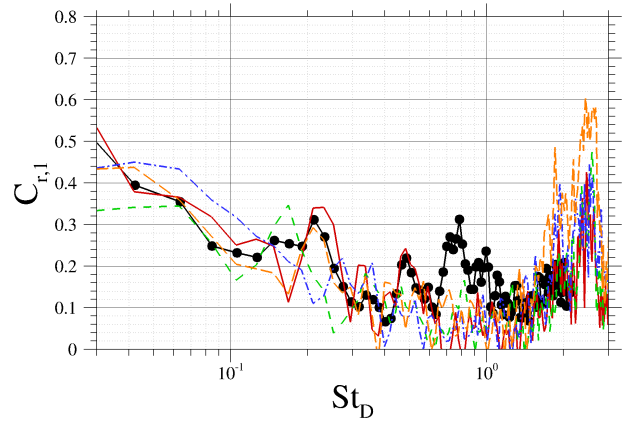
(a)



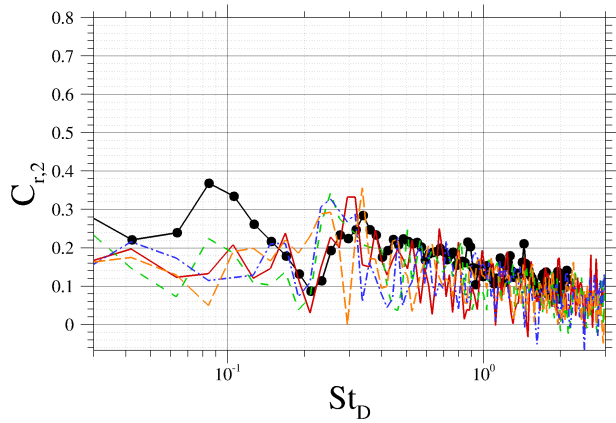
(b)



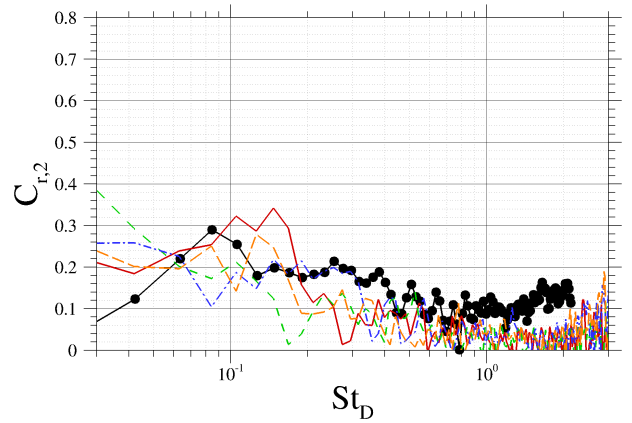
(c)



(d)



(e)



(f)

Figure 20: Spectra of the first 3 azimuthal modes for the case with jet. (a)-(c)-(e) on the extension ($x/D=0.55$). (b)-(d)-(f) on the base ($r/R=0.7$). (See Tab. 3 for computation details)

6. Conclusion

Starting from a standard, non-automatic, numerical framework for accurate RANS/LES computations of shock-free space launcher afterbody flows, we have gradually built an efficient automatic workflow adapted to turbulent flows containing shocks. This strategy is based on several numerical features. First, the implementation of a hybrid numerical scheme and a hybrid MUSCL reconstruction based on Ducros's sensor [37] enables to switch from a low-dissipation formulation in presence of vortical structures to a robust formulation in presence of high gradients. Then, the latest automatic mode of ZDES (ZDES mode 2 (2020) [35]) is used for turbulence modelling. The contributions of these features have been progressively evaluated thanks to eight ZDES computations of a transonic space launcher afterbody geometry with and without propulsive jet. Thorough comparisons with experimental measurements and standard ZDES computations have shown that, notwithstanding a minor increase of numerical diffusion in vortical regions, the proposed automatic shock-capturing RANS/LES workflow is able to retain the most of the shock-free reference framework accuracy and provides satisfying flow predictions according to an extended nomenclature for validation of simulation techniques [3]. The presented workflow thus appears well suited to accurately study realistic launcher afterbody geometries with propulsive jet(s) with a reasonable computational cost and a low user workload. As regards the overall results provided by the ZDES computations, the introduction of turbulent content within the space launcher main body boundary layer (e.g. mode 3 of the ZDES [60]) and the taking into account of the thermodynamic properties of the propulsive jet could be the next steps to further improve the prediction of pressure levels for realistic space launchers.

7. Acknowledgments

The authors wish to thank the Centre National d'Études Spatiales (CNES) for financial support. The Ph.D. work of J. Reynaud is funded by CNES and ONERA.

References

- 410 [1] D. Deprés, P. Reijasse, J. P. Dussauge, Analysis of unsteadiness in afterbody transonic flows, *AIAA Journal* 42 (12) (2004) 2541–2550. doi:10.2514/1.7000.
URL <https://doi.org/10.2514/1.7000>
- [2] D. Deprés, Analyse physique et modélisation des instationnarités dans les écoulements d’arrière-corps transsoniques, Ph.D. thesis, Aix-Marseille 2 (2003).
- 415 [3] P.-É. Weiss, S. Deck, On the coupling of a zonal body-fitted/immersed boundary method with ZDES: Application to the interactions on a realistic space launcher afterbody flow, *Computers & Fluids* 176 (2018) 338–352. doi:10.1016/j.compfluid.2017.06.015.
URL <https://doi.org/10.1016/j.compfluid.2017.06.015>
- [4] J. Delery, M. Sirieix, Base flows behind missiles, Tech. rep., AGARD LS-98 ONERA (1979).
- 420 [5] A. P. de Mirand, J.-M. Bahu, O. Gogdet, Ariane Next, a vision for the next generation of Ariane Launchers, *Acta Astronautica* 170 (2020) 735–749. doi:10.1016/j.actaastro.2020.02.003.
URL <https://doi.org/10.1016/j.actaastro.2020.02.003>
- [6] S. Deck, P. Thorigny, Unsteadiness of an axisymmetric separating-reattaching flow: Numerical investigation, *Physics of Fluids* 19 (6) (2007) 065103. doi:10.1063/1.2734996.
425 URL <https://doi.org/10.1063/1.2734996>
- [7] V. Statnikov, M. Meinke, W. Schröder, Reduced-order analysis of buffet flow of space launchers, *Journal of Fluid Mechanics* 815 (2017) 1–25. doi:10.1017/jfm.2017.46.
URL <https://doi.org/10.1017/jfm.2017.46>
- [8] P. Sagaut, S. Deck, Large Eddy Simulation for Aerodynamics: Status and perspectives, *Philosophical Transactions of the Royal Society A: Mathematical, Physical and Engineering Sciences* 367 (1899) (2009) 2849–2860. doi:10.1098/rsta.2008.0269.
430 URL <https://doi.org/10.1098/rsta.2008.0269>
- [9] T.-H.-H. Lê, Etude expérimentale du couplage entre l’écoulement transsonique d’arrière-corps et les charges latérales dans les tuyères propulsives, Ph.D. thesis, Poitiers (2005).
- 435 [10] S. Deck, E. Garnier, Detached and large eddy simulation of unsteady side-loads over an axisymmetric afterbody, in: *Fifth European Symposium on Aerothermodynamics for Space Vehicles*, Vol. 563, 2005, p. 297.
- [11] P. Meliga, P. Reijasse, Unsteady transonic flow behind an axisymmetric afterbody equipped with two boosters, in: *25th AIAA Applied Aerodynamics Conference*, American Institute of Aeronautics and Astronautics, 2007. doi:10.2514/6.2007-4564.
440 URL <https://doi.org/10.2514/6.2007-4564>

- [12] P.-É. Weiss, S. Deck, J.-C. Robinet, P. Sagaut, On the dynamics of axisymmetric turbulent separating/reattaching flows, *Physics of Fluids* 21 (7) (2009) 075103. doi:10.1063/1.3177352.
URL <https://doi.org/10.1063/1.3177352>
- [13] P.-É. Weiss, S. Deck, Control of the antisymmetric mode ($m = 1$) for high reynolds axisymmetric turbulent separating/reattaching flows, *Physics of Fluids* 23 (9) (2011) 095102. doi:10.1063/1.3614481.
445 URL <https://doi.org/10.1063/1.3614481>
- [14] M. Bitter, S. Scharnowski, R. Hain, C. J. Kähler, High-repetition-rate PIV investigations on a generic rocket model in sub- and supersonic flows, *Experiments in Fluids* 50 (4) (2010) 1019–1030. doi:10.1007/s00348-010-0988-8.
450 URL <https://doi.org/10.1007/s00348-010-0988-8>
- [15] M. Bitter, T. Hara, R. Hain, D. Yorita, K. Asai, C. J. Kähler, Characterization of pressure dynamics in an axisymmetric separating/reattaching flow using fast-responding pressure-sensitive paint, *Experiments in Fluids* 53 (6) (2012) 1737–1749. doi:10.1007/s00348-012-1380-7.
URL <https://doi.org/10.1007/s00348-012-1380-7>
- [16] V. Statnikov, T. Sayadi, M. Meinke, P. Schmid, W. Schröder, Analysis of pressure perturbation sources on a generic space launcher after-body in supersonic flow using zonal turbulence modeling and dynamic mode decomposition, *Physics of Fluids* 27 (1) (2015) 016103.
455
- [17] R. Pain, P.-E. Weiss, S. Deck, Zonal Detached Eddy Simulation of theFlow Around a Simplified Launcher Afterbody, *AIAA Journal* 52 (9) (2014) 1967–1979. doi:10.2514/1.j052743.
460 URL <https://doi.org/10.2514/1.j052743>
- [18] G. Pont, P. Cinnella, J.-C. Robinet, P. Brenner, Assessment of automatic hybrid RANS/LES models for industrial CFD, in: 32nd AIAA Applied Aerodynamics Conference, American Institute of Aeronautics and Astronautics, 2014. doi:10.2514/6.2014-2691.
URL <https://doi.org/10.2514/6.2014-2691>
- [19] F. F. J. Schrijer, A. Sciacchitano, F. Scarano, Spatio-temporal and modal analysis of unsteady fluctuations in a high-subsonic base flow, *Physics of Fluids* 26 (8) (2014) 086101. doi:10.1063/1.4891257.
465
- [20] S. Scharnowski, V. Statnikov, M. Meinke, W. Schröder, C. J. Kähler, Combined experimental and numerical investigation of a transonic space launcher wake, in: D. Knight, I. Lipatov, P. Reijasse (Eds.), *Progress in Flight Physics – Volume 7*, EDP Sciences, 2015. doi:10.1051/eucass/201507311.
470 URL <https://doi.org/10.1051/eucass/201507311>
- [21] T. Horchler, K. Oßwald, V. Hannemann, K. Hannemann, Hybrid RANS-LES study of transonic flow in the wake of a generic space launch vehicle, in: *Progress in Hybrid RANS-LES Modelling*, Springer International Publishing, 2018, pp. 291–300. doi:10.1007/978-3-319-70031-1_24.
URL https://doi.org/10.1007/978-3-319-70031-1_24

- 475 [22] P. Van Gent, From particles to pressure PIV-based pressure reconstruction for base flows, Ph.D. thesis, Delft University of Technology (2018). doi:10.4233/uuid:572bc8e5-ffc2-4562-b445-bc061fdc2f00.
- [23] S. Scharnowski, M. Bosyk, F. F. J. Schrijer, B. W. van Oudheusden, Passive flow control for the load reduction of transonic launcher afterbodies, *AIAA Journal* (jan 2019). doi:10.2514/1.j057357.
- [24] D. Saile, Experimental analysis on near-wake flows of space transportation systems, Ph.D. thesis, Deutsches
480 Zentrum für Luft-und Raumfahrt e.V. (2019).
- [25] R. Pain, P.-E. Weiss, S. Deck, J.-C. Robinet, Large scale dynamics of a high Reynolds number axisymmetric separating/reattaching flow, *Physics of Fluids* 31 (12) (2019) 125119. doi:10.1063/1.5121587.
URL <https://doi.org/10.1063/1.5121587>
- [26] F. Simon, S. Deck, P. Guillen, R. Cayzac, A. Merlen, Zonal-Detached-Eddy Simulation of Projectiles in the
485 subsonic and transonic regimes, *AIAA Journal* 45 (7) (2007) 1606–1619. doi:10.2514/1.26827.
URL <https://doi.org/10.2514/1.26827>
- [27] F. Simon, S. Deck, P. Guillen, P. Sagaut, Reynolds-Averaged Navier-Stokes/Large-Eddy Simulations of super-
sonic base flow, *AIAA Journal* 44 (11) (2006) 2578–2590. doi:10.2514/1.21366.
URL <https://doi.org/10.2514/1.21366>
- 490 [28] J. Reynaud, P. Weiss, S. Deck, Towards binary gas mixture ZDES for space launcher base flow prediction, in:
55 th 3AF International Conference on Applied Aerodynamics Poitiers – France, 2020+1.
- [29] S. Deck, Recent improvements in the Zonal Detached Eddy Simulation (ZDES) formulation, *Theoretical and
Computational Fluid Dynamics* 26 (6) (2011) 523–550. doi:10.1007/s00162-011-0240-z.
URL <https://doi.org/10.1007/s00162-011-0240-z>
- 495 [30] P. Spalart, S. Allmaras, A one-equation turbulence model for aerodynamic flows, in: 30th Aerospace Sciences
Meeting and Exhibit, American Institute of Aeronautics and Astronautics, 1992. doi:10.2514/6.1992-439.
URL <https://doi.org/10.2514/6.1992-439>
- [31] K. Hannemann, H. Ludeke, J.-F. Pallegoix, A. Ollivier, H. Lambare, J. Maseland, E. Geurts, M. Frey, S. Deck,
F. Schrijer, et al., Launch vehicle base buffeting-recent experimental and numerical investigations, in: 7th
500 European Symposium on Aerothermodynamics, Vol. 692, 2011, p. 102.
- [32] F. R. Menter, Two-equation eddy-viscosity turbulence models for engineering applications, *AIAA Journal*
32 (8) (1994) 1598–1605. doi:10.2514/3.12149.
- [33] J. B. Perot, J. Gadebusch, A self-adapting turbulence model for flow simulation at any mesh resolution, *Physics
of Fluids* 19 (11) (2007) 115105. doi:10.1063/1.2780195.
505 URL <https://doi.org/10.1063/1.2780195>
- [34] J. P. Boris, F. F. Grinstein, E. S. Oran, R. L. Kolbe, New insights into large eddy simulation, *Fluid Dynamics
Research* 10 (4-6) (1992) 199–228. doi:10.1016/0169-5983(92)90023-p.

- [35] S. Deck, N. Renard, Towards an enhanced protection of attached boundary layers in hybrid RANS/LES methods, *Journal of Computational Physics* 400 (2020) 108970. doi:10.1016/j.jcp.2019.108970.
510 URL <https://doi.org/10.1016/j.jcp.2019.108970>
- [36] M.-S. Liou, A sequel to AUSM: AUSM+, *Journal of Computational Physics* 129 (2) (1996) 364–382. doi:10.1006/jcph.1996.0256.
URL <https://doi.org/10.1006/jcph.1996.0256>
- [37] F. Ducros, V. Ferrand, F. Nicoud, C. Weber, D. Darracq, C. Gacherieu, T. Poinso, Large-eddy simulation of the shock/turbulence interaction, *Journal of Computational Physics* 152 (2) (1999) 517–549. doi:10.1006/jcph.1999.6238.
515 URL <https://doi.org/10.1006/jcph.1999.6238>
- [38] G. Zhao, M. Sun, A. Memmolo, S. Pirozzoli, A general framework for the evaluation of shock-capturing schemes, *Journal of Computational Physics* 376 (2019) 924–936. doi:10.1016/j.jcp.2018.10.013.
520 URL <https://doi.org/10.1016/j.jcp.2018.10.013>
- [39] E. Garnier, M. Mossi, P. Sagaut, P. Comte, M. Deville, On the use of shock-capturing schemes for large-eddy simulation, *Journal of Computational Physics* 153 (2) (1999) 273–311. doi:10.1006/jcph.1999.6268.
URL <https://doi.org/10.1006/jcph.1999.6268>
- [40] S. Pirozzoli, Conservative hybrid compact-WENO schemes for shock-turbulence interaction, *Journal of Computational Physics* 178 (1) (2002) 81–117. doi:10.1006/jcph.2002.7021.
525 URL <https://doi.org/10.1006/jcph.2002.7021>
- [41] C. Bogey, N. de Cacqueray, C. Bailly, A shock-capturing methodology based on adaptative spatial filtering for high-order non-linear computations, *Journal of Computational Physics* 228 (5) (2009) 1447–1465. doi:10.1016/j.jcp.2008.10.042.
530 URL <https://doi.org/10.1016/j.jcp.2008.10.042>
- [42] E. Johnsen, J. Larsson, A. V. Bhagatwala, W. H. Cabot, P. Moin, B. J. Olson, P. S. Rawat, S. K. Shankar, B. Sjögreen, H. Yee, X. Zhong, S. K. Lele, Assessment of high-resolution methods for numerical simulations of compressible turbulence with shock waves, *Journal of Computational Physics* 229 (4) (2010) 1213–1237. doi:10.1016/j.jcp.2009.10.028.
535 URL <https://doi.org/10.1016/j.jcp.2009.10.028>
- [43] S. Deck, Zonal-Detached-Eddy Simulation of the flow around a high-lift configuration, *AIAA Journal* 43 (11) (2005) 2372–2384. doi:10.2514/1.16810.
URL <https://doi.org/10.2514/1.16810>
- [44] S. Deck, R. Laroüffie, Numerical investigation of the flow dynamics past a three-element aerofoil, *Journal of Fluid Mechanics* 732 (2013) 401–444. doi:10.1017/jfm.2013.363.
540 URL <https://doi.org/10.1017/jfm.2013.363>

- [45] G. Pont, D. Puech, P. Brenner, Hybrid RANS/LES simulation of a space launcher using a high order finite volume scheme and grid intersections technique, in: *Symposium on Hybrid RANS-LES Methods*, Springer, 2016, pp. 347–356.
- 545 [46] P. Guillen, M. Dormieux, Design of a 3D multidomain Euler code, in: *Supercomputing in fluid flow*, 1993, pp. 21–39.
- [47] M. Pechier, *Prévisions numériques de l’effet Magnus pour des configurations de munitions*, Ph.D. thesis, Poitiers (1999).
- [48] M. Pechier, P. Guillen, R. Cayzac, Magnus effect over finned projectiles, *Journal of Spacecraft and Rockets* 38 (4) (2001) 542–549.
- 550 [49] L. Manueco, P.-É. Weiss, S. Deck, On the coupling of wall-model immersed boundary conditions and curvilinear body-fitted grids for the simulation of complex geometries, *Computers and Fluids* (in revision) (2020).
- [50] I. Mary, P. Sagaut, Large Eddy Simulation of Flow Around an Airfoil Near Stall, *AIAA Journal* 40 (6) (2002) 1139–1145. doi:10.2514/2.1763.
- 555 URL <https://doi.org/10.2514/2.1763>
- [51] B. Koren, A robust upwind discretization method for advection, diffusion and source terms, in: *Numerical methods for advection-diffusion problems*, Vieweg, 1993, pp. 117–138.
- [52] E. Goncalvès, *Résolution numérique des équations d’Euler monodimensionnelles*, Lecture notes, Institut National Polytechnique de Grenoble (2004).
- 560 [53] N. Chauvet, *Simulation numérique et analyse physique d’un jet propulsif contrôlé par des injections radiales*, Ph.D. thesis, Poitiers (2007).
- [54] B. Van Leer, MUSCL, a new approach to numerical gas dynamics., in: *Computing in Plasma Physics and Astrophysics*, 1976.
- [55] P. K. Sweby, High resolution schemes using flux limiters for hyperbolic conservation laws, *SIAM journal on numerical analysis* 21 (5) (1984) 995–1011.
- 565 [56] R. Collercandy, An improved approach for the computation of transonic/supersonic flows with applications to aerospace configurations, in: *10th Applied Aerodynamics Conference*, American Institute of Aeronautics and Astronautics, 1992. doi:10.2514/6.1992-2613.
- URL <https://doi.org/10.2514/6.1992-2613>
- 570 [57] Arianespace, *Ariane 6 user’s manual*, Tech. rep. (2018).
- [58] P. L. van Gent, Q. Payanda, S. G. Brust, B. W. van Oudheusden, F. F. J. Schrijer, Effects of exhaust plume and nozzle length on compressible base flows, *AIAA Journal* 57 (3) (2019) 1–16. doi:10.2514/1.j057314.

- [59] P. Catalano, M. Marini, A. Nicoli, A. Pizzicaroli, Cfd contribution to the aerodynamic data set of the vega launcher, *Journal of Spacecraft and Rockets* 44 (1) (2007) 42–51.
- 575 [60] S. Deck, N. Renard, R. Laroche, P. Sagaut, Zonal Detached Eddy Simulation (ZDES) of a spatially developing flat plate turbulent boundary layer over the reynolds number range $3\,150 \leq Re_\theta \leq 14\,000$, *Physics of Fluids* 26 (2) (2014) 025116.
- [61] S. Deck, A. T. Nguyen, Unsteady side loads in a thrust-optimized contour nozzle at hysteresis regime, *AIAA journal* 42 (9) (2004) 1878–1888.